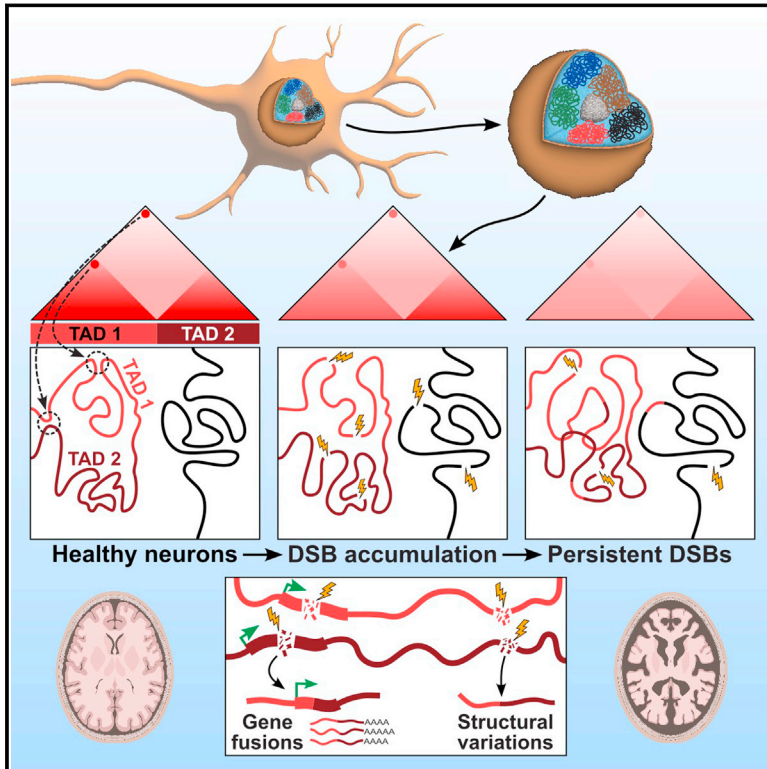


# Neuronal DNA double-strand breaks lead to genome structural variations and 3D genome disruption in neurodegeneration

## Graphical abstract



## Authors

Vishnu Dileep, Carles A. Boix, Hansruedi Mathys, ..., David A. Bennett, Manolis Kellis, Li-Huei Tsai

## Correspondence

vdileep@mit.edu (V.D.),  
manoli@mit.edu (M.K.),  
lhtsai@mit.edu (L.-H.T.)

## In brief

Disruption of genome stability and 3D genome organization by DNA double-strand breaks in neurons are pathological steps in the progression of neurodegeneration.

## Highlights

- Increased somatic mosaic gene fusions in excitatory neurons in Alzheimer's disease
- DNA double-strand breaks lead to mosaic gene fusions and genome structural variations
- Changes in 3D genome organization in neurons enriched for DNA double-strand breaks
- 3D genome changes align with differential gene expression in neurodegeneration



Article

# Neuronal DNA double-strand breaks lead to genome structural variations and 3D genome disruption in neurodegeneration

Vishnu Dileep,<sup>1,2,6,\*</sup> Carles A. Boix,<sup>4,6</sup> Hansruedi Mathys,<sup>1,2</sup> Asaf Marco,<sup>1,2</sup> Gwyneth M. Welch,<sup>1,2</sup> Hiruy S. Meharena,<sup>1,2</sup> Anjanet Loon,<sup>1,2</sup> Ritika Jeloka,<sup>1,2</sup> Zhuyu Peng,<sup>1,2</sup> David A. Bennett,<sup>5</sup> Manolis Kellis,<sup>3,4,\*</sup> and Li-Huei Tsai<sup>1,2,3,7,\*</sup>

<sup>1</sup>Picower Institute for Learning and Memory, Massachusetts Institute of Technology, Cambridge, MA 02139, USA

<sup>2</sup>Department of Brain and Cognitive Sciences, Massachusetts Institute of Technology, Cambridge, MA 02139, USA

<sup>3</sup>Broad Institute of MIT and Harvard, Cambridge, MA 02142, USA

<sup>4</sup>Computer Science and Artificial Intelligence Laboratory, Massachusetts Institute of Technology, Cambridge, MA, USA

<sup>5</sup>Rush Alzheimer's Disease Center, Chicago, IL, USA

<sup>6</sup>These authors contributed equally

<sup>7</sup>Lead contact

\*Correspondence: [vdileep@mit.edu](mailto:vdileep@mit.edu) (V.D.), [manoli@mit.edu](mailto:manoli@mit.edu) (M.K.), [lhtsai@mit.edu](mailto:lhtsai@mit.edu) (L.-H.T.)

<https://doi.org/10.1016/j.cell.2023.08.038>

## SUMMARY

Persistent DNA double-strand breaks (DSBs) in neurons are an early pathological hallmark of neurodegenerative diseases including Alzheimer's disease (AD), with the potential to disrupt genome integrity. We used single-nucleus RNA-seq in human postmortem prefrontal cortex samples and found that excitatory neurons in AD were enriched for somatic mosaic gene fusions. Gene fusions were particularly enriched in excitatory neurons with DNA damage repair and senescence gene signatures. In addition, somatic genome structural variations and gene fusions were enriched in neurons burdened with DSBs in the CK-p25 mouse model of neurodegeneration. Neurons enriched for DSBs also had elevated levels of cohesin along with progressive multiscale disruption of the 3D genome organization aligned with transcriptional changes in synaptic, neuronal development, and histone genes. Overall, this study demonstrates the disruption of genome stability and the 3D genome organization by DSBs in neurons as pathological steps in the progression of neurodegenerative diseases.

## INTRODUCTION

DNA damage and defective DNA repair are hallmarks of aging and several neurodegenerative disorders including Alzheimer's disease (AD).<sup>1–3</sup> Neurons are generally post-mitotic cells that can last the life span of an organism, making them especially vulnerable to the accumulation of DNA repair defects. Studies using postmortem human brain samples show that neurons, astrocytes, and oligodendrocytes accumulate DNA double-strand breaks (DSBs) early in the progression of AD.<sup>2,4–7</sup> In addition to pathological sources of DNA breaks, neurons also actively induce both DSBs and single-stranded breaks as part of their normal physiology.<sup>8–11</sup> Further, extensive active demethylation following neuronal activity through the Tet-TDG pathway-associated base excision repair can also be a source of DNA breaks.<sup>8,12,13</sup> While several studies have focused on understanding DNA repair mechanisms in AD, only a few studies have attempted to understand the epigenetic consequences of DSBs in AD.<sup>2,14,15</sup>

Persistent DSBs are drivers of genomic instability.<sup>16</sup> The major repair pathway that resolves DSBs in neurons is the non-homol-

ogous end-joining (NHEJ).<sup>17</sup> However, NHEJ is error-prone and can cause genome structural variations, potentially leading to gene fusions with pathological gain or loss of function.<sup>18–20</sup> These pathological effects of structural variations are well demonstrated in various cancers.<sup>21,22</sup> In addition, structural variations have the potential to rewire genes with ectopic regulatory elements.<sup>23–25</sup> Therefore, the observation that DSBs accumulate in neurons in the early stages of AD begs the question of whether these DSBs lead to genome structural variations in neurons.<sup>26</sup>

The genome is hierarchically organized at different scales within the nucleus. Chromatin interactions including chromatin loops form self-interacting topologically associating domains (TADs) that spatially segregate in the nucleus to give rise to the transcriptionally active and repressive compartments. This organization of the genome is closely associated with several fundamental biological paradigms including gene expression, DNA replication, genome stability, DNA repair, development, cell cycle, antibody repertoire generation by V(D)J recombination, etc., to name a few among the growing list of processes regulated by the 3D folding of the genome.<sup>27–35</sup> There is now



emerging evidence that the 3D genome is actively regulated during learning and memory formation.<sup>36–41</sup> Further, the disruption of 3D genome organization has been demonstrated in neurodevelopmental disorders such as Fragile X syndrome and Down syndrome, etc.<sup>42,43</sup> Chromatin accessibility has also been shown to be disrupted in the AD brain.<sup>44,45</sup> Other studies have demonstrated how disease-associated SNPs in non-coding areas of the genome influence genes associated with diseases including AD.<sup>46–50</sup> DSBs have the potential to directly affect the 3D genome organization.<sup>51–54</sup> Persistent DSBs in neurons could also indirectly impact the 3D genome organization through genome structural variations.<sup>55,56</sup>

To explore the genomic consequences of DSBs in AD, we used both human postmortem brain samples and a mouse model of neurodegeneration that recapitulate the pre-symptomatic accumulation of DSBs. We show increased gene fusions, genome structural variations, and changes in 3D genome organization in neurons harboring DSBs. Our results demonstrate the disruption of genome stability and the 3D genome organization mediated by DSBs as pathological steps in the progression of neurodegenerative diseases.

## RESULTS

### DSB-bearing neurons have mosaic genome structural variations in neurodegeneration

We obtained postmortem human prefrontal cortex brain samples from 47 Religious Orders Study and Rush Memory and Aging Project (ROSMAP) participants and classified them into 23 non-pathologic AD individuals (NIA-Reagan 3–4) and 24 individuals with pathologic AD (NIA-Reagan 1–2). We used well-based single-nucleus RNA-seq full-transcript profiles (snRNA-seq, Smart-Seq2 v2.032) across all 47 individuals and obtained 6,180 cells (5,421 after QC) (Figures 1A, S1A, and S1B; Table S1, page 1).<sup>57</sup> We used known marker gene expression to annotate 2,121 oligodendrocytes (39.1%), 1,170 excitatory neurons (21.6%), 255 microglia (4.7%), 221 inhibitory neurons (4.1%), 220 astrocytes (4.1%), 94 OPCs (1.7%), and 40 endothelial cells (0.7%) (Table S1, page 2). We also identified a cluster of 1,300 cells (24%) that we refer to here as “unidentified/dying” with reduced transcription and loss of cell-type-identity markers, positioned between neurons and oligodendrocytes in the two-dimensional t-SNE cell embedding. This cluster also had a lower number of reads and genes per cell, indicating that they are unlikely to be doublets (Figure S1C).

We then called mosaic gene fusion events in each cell independently, using STAR-fusion to detect chimeric snRNA-seq reads mapping between two genes as a proxy for genome structural variations (Table S1, page 3).<sup>58</sup> As expected, the majority of cells did not have any gene fusions, and 95% of the cells with gene fusions had between 1 and 4 fusion events (Figure S1D). Only 3.3% of pairs of genes involved in intra-chromosomal fusions were adjacent to each other, making gene fusions due to RNA polymerase run-through unlikely as a major source of false positives (Figures S1E and S1F). We quantified enrichments of putative fusion events across multiple conditions using a negative binomial regression framework controlling for cell quality and individual-level covariates including postmortem

interval, sex, and age of death. Strikingly, we found that gene fusions were significantly enriched in cells from individuals with AD pathology as ascertained by the NIA-Reagan score (pathology diagnosis, AD = 1–2 and non-AD = 3–4) relative to cells from non-AD individuals (adjusted p value = 0.046). We also found that gene fusions were significantly enriched in cells from late-AD individuals, as defined by the presence of neurofibrillary tangles (NFTs) in their prefrontal cortex (Braak stages 5–6 versus non/early-AD stages 1–4, adjusted p value = 0.00031) (Figure 1B). Stratifying the gene fusion enrichment by cell type revealed that excitatory neurons in particular were enriched for gene fusions and that they showed a higher effect size compared to all other cell types in late AD individuals (Figures 1B and S1G). To validate these results in a second cohort of individuals, we used 10x snRNA-seq data for over 2 million cells from 380 individuals (profiled in the accompanying Mathys et al. study<sup>60</sup>). We re-aligned and called fusions on the 10x snRNA-seq reads to detect gene fusion junctions involving the 3' end of the 10x cDNA molecule. Repeating the analysis done in the Smart-seq2 cohort, we observed significantly increased gene fusion events (adjusted p value < 0.001) in cells from AD individuals compared to non-AD individuals as ascertained by NIA-Reagan and Braak stage (late-AD versus non/early-AD) (Figure 1B; Table S1, page 4).

Since genome structural variations can result from errors in DNA repair and as DNA repair pathways can be up-regulated in the presence of DNA damage, we asked whether cells with increased activity of specific damage-associated and normal neuronal genes showed different gene fusions burden.<sup>61</sup> We scored all cells in the Smart-seq2 and 10x datasets by their expression of genes involved in functional pathways (GO) related to DNA damage, repair, senescence, neuronal, and synaptic functions. Excitatory neurons with higher expression of DNA damage, repair, and senescence-associated gene sets (Table S1, page 5) showed a significant increase in their gene fusion burden in the 10x dataset (Figure 1C). On the other hand, excitatory neurons with higher expression of genes associated with neuronal identity and synaptic function were depleted for gene fusions in both datasets (Figure 1C). Analyzing all cells jointly showed significant effects in the same directions but with reduced effect sizes (in the 10x data) for the enrichment of fusions in repair, DNA damage, and senescence-associated cells (Figure 1C). The increased mosaic gene fusion burden in cells with these expression profiles suggests that DNA breaks in neurons could potentially lead to a senescence-like state with increased genome structural variations. DNA damage-related gene expression in excitatory neurons was associated with several key measures of AD pathology in our 10x data, in line with previous studies that found a link between DNA damage and AD (Figure S1H).<sup>2,4–7</sup>

To investigate the genomic impact of DSBs in neurons, we utilized the CK-p25 mouse model of inducible and synchronous neurodegeneration which recapitulates the pre-symptomatic accumulation of DSBs and expression of senescence-associated genes in excitatory neurons.<sup>58</sup> By using this model, we were able to isolate neurons at different states of DSB accumulation, enabling us to more accurately assess the effects of DSBs on genome integrity. In these mice, the expression of p25, an

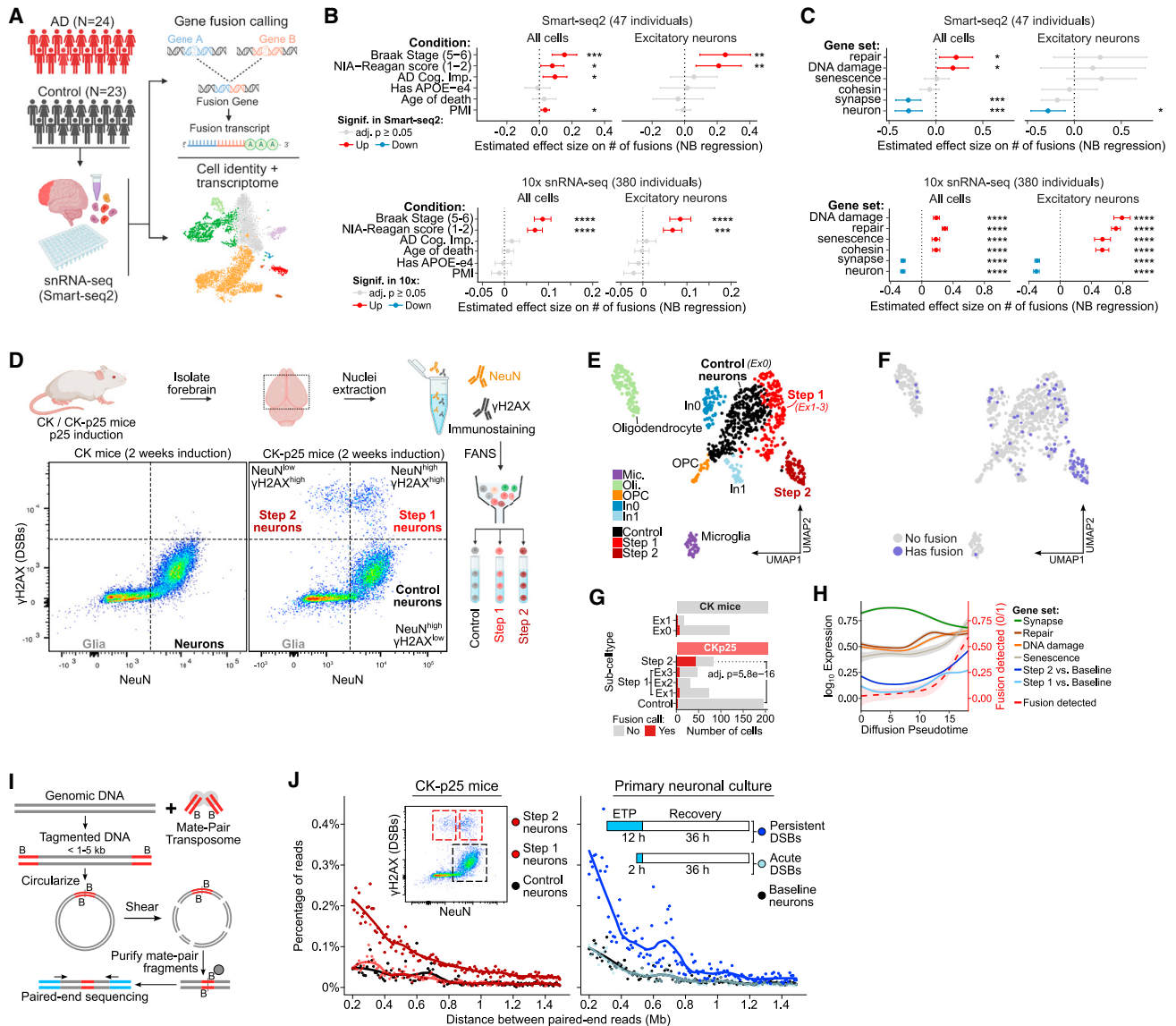


**Figure 1. DSBs in neurons lead to mosaic genome structural variations**

(A) Schematic of snRNA-seq (Smart-seq2) analysis in human postmortem brains.

(B) The effect size of the number of gene fusions using human snRNA-seq as a function of human sample covariates. Significantly increased (red) or decreased (blue) gene fusions shown for adjusted p value < 0.05. Human sample covariates include AD cognitive impairment score (AD Cog, Imp) and postmortem interval (PMI) (\*  $p < 0.05$ , \*\*  $p < 0.01$ , \*\*\*  $p < 1e-3$ , \*\*\*\*  $p < 1e-4$ , error bars are 2\*SE).

(C) The effect size of the number of gene fusions as a function of gene sets associated with different Gene Ontology (GO) terms, similar to (B).

(D) Representative FANS dot-plot of CK/CK-p25 forebrain after 2 weeks induction using NeuN (neuron) and  $\gamma$ H2AX (DSB) marker.

(E) UMAP embedding of CK/CK-p25 snRNA-seq after 1 or 2 weeks of induction. Colors indicate cell-type annotations. Control neurons (Ex0) and Step 1 neurons are represented by clusters Ex1, Ex2, and Ex3.

(F) Overlay of cells containing at least 1 gene fusion event (blue) on the snRNA-seq UMAP embedding.

(G) Quantification of the number of cells with at least one gene fusion and the total number of cells for Control, Step 1 (Ex1, Ex2, Ex3 clusters), and Step 2. Significance from Fisher's exact test between Control and Step 2 in CKp25 mice.

(H) Trajectory analysis of Control, Step 1, and Step 2. Lines indicate the fraction of cells with gene fusions (dotted red lines) or smoothed expression of gene sets along the pseudo-time trajectory. Step 1 and Step 2 gene sets are defined as significantly upregulated genes from Step 1 vs. Control and Step 2 vs. Control comparisons from bulk RNA-seq (Welch et al. 53), respectively (adjusted p value < 0.05,  $\log_2$  fold-change  $\geq 1.0$ ).

(I) Schematic of mate-pair sequencing. Genomic DNA is tagged to sizes between 1 and 5 kb with Tn5 transposase carrying biotinylated adaptors. The fragments are circularized and then sheared into 200–300 bp fragments. The ligation junctions are then enriched through biotin pull-down and

(legend continued on next page)



activator of cyclin-dependent kinase 5 (Cdk5), is under the control of the *CamKII* promoter and can be switched on by withdrawing doxycycline from the animal's diet through doxycycline (dox)-off system.<sup>62</sup> In CK-p25, DSB accumulation starts at 1 week, with maximum levels of DSB at 2 weeks after the removal of doxycycline.<sup>63</sup> Thereafter, intracellular amyloid-beta accumulation occurs as early as 2–3 weeks after induction.<sup>64</sup> Neuronal loss, learning deficits, and tau hyperphosphorylation are also observed between 4 to 12 weeks after doxycycline removal.<sup>62,64</sup> Using fluorescence-activated nuclei sorting (FANS), we can isolate three distinct populations of neuronal nuclei using pan-nuclear neuronal marker NeuN and DSBs marker  $\gamma$ H2AX. After 2 weeks of p25 induction in CK-p25 mice, we isolated (1) neurons with high levels of NeuN and baseline levels of  $\gamma$ H2AX (Control neurons), (2) neurons with high levels of NeuN and  $\gamma$ H2AX (Step 1 neurons), and (3) cells with low levels of NeuN and high levels of  $\gamma$ H2AX (Step 2 neurons) (Figure 1D). We previously showed that Step 2 neurons are indeed neurons that enter a later step of neurodegeneration that is characterized by the expression of senescence and immune genes.<sup>58</sup>

We used the previously published snRNA-seq in CK-p25 mice to test if neurons enriched for  $\gamma$ H2AX have increased levels of gene fusions as a proxy for increased genome structural variation. Single-nucleus RNA-seq (Smart-seq2) was performed on all four FANS gates (Control neurons, NeuN<sup>high</sup>  $\gamma$ H2AX<sup>low</sup>; Glia, NeuN<sup>low</sup>  $\gamma$ H2AX<sup>low</sup>; Step 1 neurons, NeuN<sup>high</sup>  $\gamma$ H2AX<sup>high</sup>; and Step 2 neurons, NeuN<sup>low</sup>  $\gamma$ H2AX<sup>high</sup>) from both CK and CK-p25 mice induced for 1 or 2 weeks. Step 2 neurons from CK-p25 mice formed a distinct expression cluster, whereas Step 1 was distributed into three clusters (Ex1, Ex2, and Ex3) between the Control (Ex0) and Step 2 clusters on a UMAP representation of the cells (Figure 1E). Step 2 neurons were significantly enriched for gene fusion calls ( $p$  value =  $5.8e^{-16}$ ), whereas Step 1 neurons showed a modest increase in gene fusions ( $p$  value > 0.05) (Figures 1F, 1G, and S2A–S2C; Table S1, page 6). We used Monocle 3 to order Control, Step 1, and Step 2 neuron nuclei along a gene expression pseudotime trajectory.<sup>65</sup> As we previously described, signatures of the Step 1 state (from comparing Step 1 vs. Control bulk RNA-seq) increased from Control to Step 1 and then plateaued, whereas the signatures of Step 2 (from comparing Step 2 vs. Control bulk RNA-seq) neurons continue to increase into Step 2 neurons as a function of pseudo time.<sup>58</sup> Remarkably, gene fusion frequency increased as a function of pseudo time, along with genes associated with senescence, similar to the Step 2 signature. On the other hand, genes associated with DNA damage and repair increased and plateaued similar to the Step 1 signature (Figures 1H, S2D, and S2E). These results show that neurons with increased DSB burden (Step 1) progress to a senescence-like state that is characterized by increased gene fusions (Step 2).

We wondered whether increased gene fusions are the result of a general increase in genome-wide genome structural variations. To test this, we performed long-insert mate-pair sequencing to

detect structural variations genome-wide. Here, genomic DNA was fragmented by Tn5 transposase carrying biotinylated adaptors. The fragments were circularized and then sheared into 200–300 bp fragments. The ligation junctions were then enriched through biotin pull-down and paired-end sequenced (Figure 1I). We first performed mate-pair sequencing in neurons with baseline levels of  $\gamma$ H2AX and in  $\gamma$ H2AX<sup>high</sup> neurons. Since the insert size was centered around 1–5 kb, pairs of reads that are separated by much larger distances would indicate genome structural variations. As expected, the vast majority of the read pairs ( $95.4 \pm 0.9\%$ ) were separated by a distance of less than 10 kb. To measure structural variations with high confidence, we examined the percentage of reads in each sample separated by distances of 0.2–1.5 Mb. We saw a modest increase (22% increase) in the frequency of structural variations in  $\gamma$ H2AX<sup>high</sup> neurons compared to neurons with baseline levels of  $\gamma$ H2AX (Figure S2F). Remarkably, mate-pair sequencing in  $\gamma$ H2AX<sup>high</sup> neurons partitioned into Step 1 and Step 2 revealed that Step 2 neurons had a much higher frequency of structural variation events (241% increase), whereas the structural variation frequency of Step 1 neurons was similar to that of Control neurons (Figure 1J). Structural variation frequencies follow chromosome spatial organization and tend to decay exponentially with the increasing genomic distance between the translocated loci.<sup>30,66,67</sup> Consistent with this, structural variation frequencies in all samples decreased as a function of distance (Figure 1J). These results suggest that the persistent DSBs and delayed repair in Step 1 neurons may increase the chance of repair errors and cause them to transition into Step 2 neurons with increased genome structural variations.

Next, we tested if inducing DSBs through an alternate mechanism would induce genome structural variations in neurons. We treated primary cortical neurons with etoposide (5  $\mu$ M), a topoisomerase IIb poison that induces widespread DSBs. To model the acute vs. persistent DSBs, we treated mouse primary cortical neurons with etoposide for either 2 h (acute DSBs) or 12 h (persistent DSBs) and allowed the neurons to recover in a basal etoposide-free media for 36 h. Mate-pair sequencing revealed that neurons with acute DSBs had similar levels of structural variations compared to DMSO-treated baseline neurons, whereas neurons with persistent DSBs had a markedly higher frequency of structural variation (201% increase) similar to that of the increase observed in Step 2 neurons (Figure 1J). The 2 h of treatment with etoposide was sufficient to induce DSBs, as measured by  $\gamma$ H2AX staining (Figure S2G), but not sufficient to accumulate structural variation (Figure 1J). Together, these results show that delayed repair due to persistent DSBs in excitatory neurons leads to the accumulation of mosaic genome structural variation.

#### Highly expressed genes and long genes are vulnerable sites of genome structural variations

We found that fusion genes from Control, Step 1, and Step 2 neurons had significantly higher expression (from bulk RNA-seq)

paired-end sequenced. Mapped read pairs will be separated by 1–5 kb and large deviations from the expected separation indicates genome structural variation events.

(J) Plots of mate-pair sequencing quantifying the percentage of read pairs separated by large genomic distances greater than 200 kb that indicate genome structural variation events.

See also Figure S1, S2 and Table S1, pages 1–6.

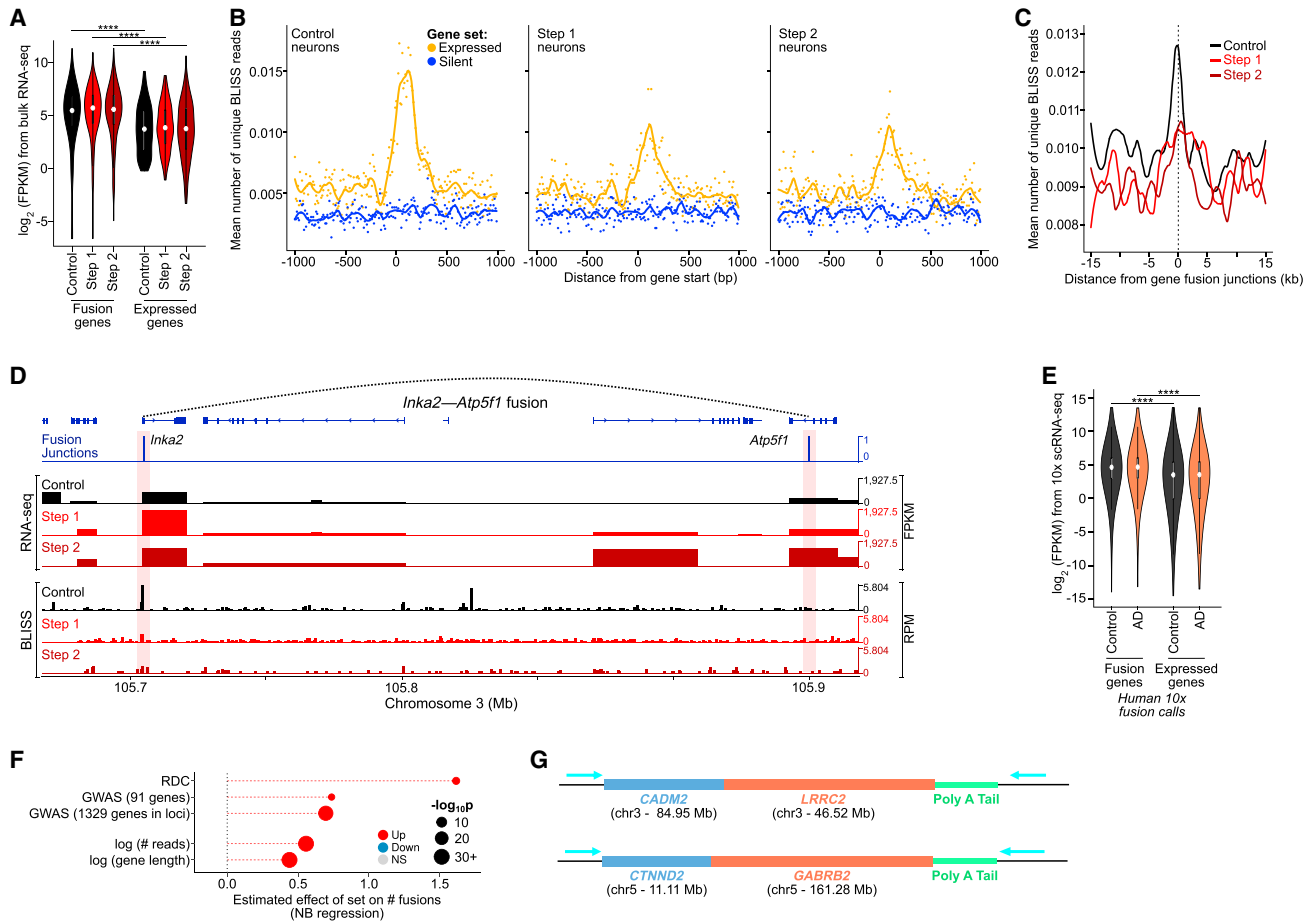


**Figure 2. Highly expressed genes and long genes are vulnerable sites for genome structural variations in neurons**

(A) Expression level of genes involved in CK-p25 gene fusions (Wilcoxon test with Benjamini–Hochberg correction, \*\*\*\* $p < 1e-4$ ).  
 (B) Aggregate plots of BLISS reads centered at gene starts for the top 2,500 expressed (yellow) and the bottom 2,500 silent genes (blue), for Control, Step 1, and Step 2 neurons.  
 (C) Aggregate plots of BLISS reads centered at gene fusion junctions called by snRNA-seq in CK-p25 neurons.  
 (D) Genome browser snapshot of example gene fusion in CK-p25 mice Step 2 neurons. Panels show fusion junctions (top), bulk RNA-seq signal (2–4), and BLISS in the three populations (5–7).  
 (E) Expression level of genes involved in human gene fusions (10x snRNA-seq) vs. all expressed genes (Wilcoxon test with BH correction).  
 (F) Effect size of the number of gene fusions as a function of genes identified as RDC gene, AD GWAS genes, gene expression level (reads), and gene length (bp).  
 (G) Schematics of example gene fusions identified through ONT long-read cDNA sequencing.  
 See also [Figure S3](#), [Table S1](#), pages 1–4, 6, 7, and 17.

than expressed genes in neurons, suggesting that increased transcription is associated with increased genome structural variation ([Figure 2A](#)).<sup>58</sup> This is consistent with the finding that genome structural variation induced by Top2B DNA breakage is dependent on transcription.<sup>68</sup> Next, we mapped DSBs directly using Break Labeling *in situ* and sequencing (BLISS) in Control, Step 1, and Step 2 neurons and found that higher gene expression was strongly associated with increased DSBs across Control, Step 1, and Step 2 neurons ([Figures 2B](#) and [S3A](#)).<sup>69</sup> Surprisingly, the level of enrichment of DSBs at highly transcribed genes was lower in Step 1 and Step 2 neurons compared to Control. This suggested that, while highly transcribed genes were hotspots for DSBs, the increased DSBs in Step 1 are distributed stochastically across the genome. BLISS uses unique molecular

identifiers (UMIs) to differentiate between independent DSB events and PCR duplicates. Therefore, conserved DSB locations across cells (hotspots) will be associated with multiple UMIs, whereas stochastic DSBs will be supported by fewer UMIs. Consistent with increased stochastic DSBs, Step 1 DSBs have fewer UMIs per genomic location. Interestingly, Step 2 neurons had a UMI distribution closer to Control, suggesting partial repair of stochastic DSBs gained in Step 1 leading to possible mosaic structural variations ([Figure S3B](#)). Finally, we observed enrichment of DSBs at the gene fusion junctions with the highest enrichment in Control cells, indicating gene-fusion junctions are frequent DSB locations ([Figure 2C](#)). Example top gene fusion calls (*Inka2–Atp51* and *Cdip1–Ubald1*), based on the number of fusion junction-spanning fragments, show increased gene

expression and DNA breakpoints at the fusion junctions (Figures 2D and S3C). Interestingly, *Inka2* and *Cdip1* are targets of p53, an important regulator of senescence, and their transcriptional disruption through genome structural variation may promote a senescent-like state.<sup>70–72</sup>

Similar to our observations from BLISS in CK-p25, human fusion genes in excitatory neurons also tended to have increased gene expression in both AD and control individuals (Figure 2E). We saw a significant overlap between genes involved in fusions and a set of actively transcribed, long neural genes that are important for synaptic function and cell-cell adhesion and are known to harbor recurrent DSB clusters (RDC) in neural precursor cells (Figure 2F).<sup>73</sup> We found 25 of the 27 recurrent DSB cluster (RDC) genes in human excitatory gene fusion calls, including *CTNND2*, *LSAMP*, and *NRXN1* (Table S1, page 7). The length and active transcription of these RDC genes likely drive their increased propensity for DSBs and gene fusions. Across all genes, both higher transcription levels and increased gene length were significantly associated with increased gene fusions (Figure 2F). The association between gene length and gene fusions was observed in mouse neurons and is consistent with increased DSBs at highly transcribed genes and long genes (Figures 2A, S3D, and S3E). Interestingly, genes linked to AD by genome-wide association studies (GWASs) were significantly longer than expected (Figure S3F) and were significantly enriched within fusion genes (Figure 2F; Table S1, page 7).<sup>74</sup> We also found a significant association between fusion genes and a larger list of genes linked to AD by GWAS and polygenic risk scores (Figure 2F) (NHGRI-EBI GWAS Catalog, ID: MONDO\_0004975).<sup>75</sup>

Finally, to validate fusion events observed by short-read sequencing, we performed Oxford Nanopore Technologies (ONT) long-read sequencing of cDNA from two AD postmortem samples. We identified several gene fusions which also included RDC genes (e.g., *CADM2*, *CTNND2*) (Figures 2G and S3G). Taken together, these results show that increased DNA breaks associated with long genes and highly transcribed genes make them vulnerable to structural variation and gene fusion.

### Neurons burdened with DSBs are associated with the disruption of 3D genome organization

In parallel, we identified a significant elevation in cohesin complex expression along with a coordinated increase in DNA damage response in excitatory neurons from subjects with high AD pathology in the large-scale snRNA-seq across 427 AD and control individuals from our companion manuscript.<sup>60</sup> The cohesin complex is an important architectural protein that organizes the 3D genome and is also important in DSB repair.<sup>32,76–78</sup> In particular, cohesin has been shown to protect against genome structural variations.<sup>79,80</sup> Further, loop extrusion mediated by cohesin and CTCF mediates the formation of chromatin loops and self-interacting TADs.<sup>77,81–84</sup> To directly investigate the levels of the cohesin complex in excitatory neurons with DSBs, we stained the CK-p25 hippocampus for the cohesin subunit RAD21 after 2 weeks of induction. RAD21 was significantly enriched in neurons with DSBs compared to those with baseline DSBs (Figure 3A). Interestingly, snRNA-seq revealed increased gene expression of another nuclear architectural protein Lamin

B1 (*Lmnb1*) in Step 1 neurons and a subsequent decrease in expression from Step 1 to Step 2 (Figure S2E). Lamin B1 plays a crucial role in the 3D genome organization by tethering heterochromatin to the nuclear periphery.<sup>85</sup> Additionally, Lamin B1 has been shown to control the release of DSB repair protein 53BP1 and overexpression of LaminB1 impeded DSB repair leading to persistent DSBs.<sup>86</sup> Immunohistochemistry of Lamin B1 in CK-p25 mice induced for 2 weeks revealed increased Lamin B1 and abnormalities in the structure of Lamin B1 in neurons bearing DSBs. Thereafter, Lamin B1 intensity decreased after 6 weeks of induction, consistent with the snRNA-seq (Figures S4A–S4C). Indeed, we show decreased Lamin B1 in late-stage human AD associated with high epigenomic erosion in our companion manuscript (Xiong et al.<sup>87</sup>).

To investigate if DSBs and the alterations in chromatin structural proteins can impact the 3D genome organization, we performed *in situ* Hi-C<sup>88</sup> in Control, Step 1, and Step 2 neurons. Hi-C revealed genome-wide alterations in the 3D genome organization that involved both gain and loss of long-range interactions (Figures 3B and 3C). Overall, there was a net decrease in the intensity of long-range interactions above 1 Mb in Step 1 neurons. This was even more pronounced in Step 2 neurons with the intensity of long-range interactions decreasing from 0.5 Mb (Figure S4E). Chromosomes are spatially segregated into generally active A compartment and repressive B compartment.<sup>89</sup> While the A compartment is largely localized to the nuclear interior, the B compartment is tethered to the nuclear periphery by Lamin B1.<sup>90</sup> Surprisingly, despite the disruption of Lamin B1, the nuclear A to B compartmentalization derived from Hi-C was largely intact. However, approximately 8.5% of the genome shifted compartments and these changes were generally progressive from Step 1 to Step 2 (Figures S4F and S4G; Table S1, page 8).

Since chromatin is organized into loops and self-interacting units called TADs by cohesin and CTCF, we wondered how DSBs and the misregulation of cohesin would affect loop and TAD organization. We used a metric called inclusion ratio that measures the ratio between intra-TAD interactions to outside-TAD interactions to quantify changes in TAD definition genome-wide.<sup>91</sup> This analysis revealed an overall significant decrease in the TAD definitions in Step 1 that was exacerbated in Step 2 (Figures 3D and 3E; Table S1, page 9). Remarkably, the accompanying manuscript by Xiong et al. describes widespread changes in cell-type specific chromatin accessibility within excitatory neurons in human AD samples which they term “epigenome erosion”.<sup>87</sup> This highlights the deterioration of chromatin structure and organization as a general pathological step in AD progression.

We also observed the disruption of chromatin loops in Step 1 and Step 2 neurons compared to control neurons (Figure 3F; Table S1, page 10). Aggregate plots of loops show genome-wide disruption of loops involving both reduction and gain of loop intensity (Figure 3G). Overall, more loops showed a reduction than a gain in intensity, and loop loss was much more pronounced in Step 2 than in Step 1 neurons (Figure 3H). Given the overall reduction in loop intensities, we wondered if loop boundaries are generally hotspots of DSBs in neurons. We found an enrichment of DSBs at loop boundaries in Control, Step 1, and Step 2 (Figure 3I). This aligns well with the observation that loop boundaries are hotspots for TOP2 B-mediated DNA breaks

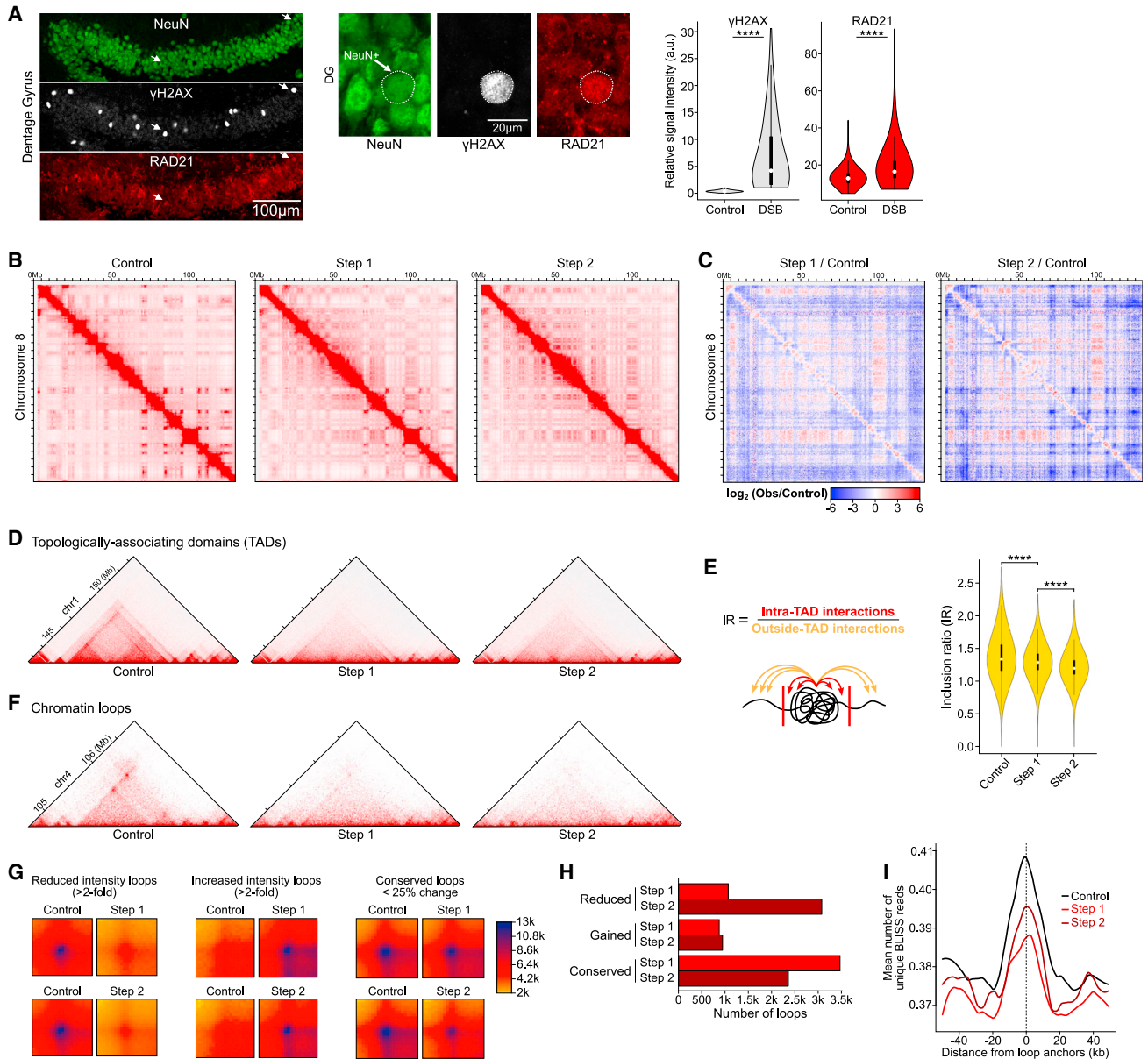


**Figure 3. Neurons burdened with DSBs exhibit global disruption of the 3D genome organization at multiple scales**

(A) Representative immunohistochemistry images and quantification of RAD21 (cohesin subunit) in 2-week-induced CK-p25 mice, comparing neurons with baseline DSBs to neurons enriched for DSBs. Representative images show dentate gyrus (left) and higher-magnification images (right). Violin plots quantify RAD21 levels between neuronal nuclei with baseline DSBs ( $\gamma$ H2AX relative intensity < 1) and neurons enriched for DSBs ( $\gamma$ H2AX relative intensity > 1) (Wilcoxon test, \*\*\*\* $p < 1e-4$ ). The mean relative intensity of  $\gamma$ H2AX (gray) and RAD21 (red) was measured within NeuN surfaces. Control (n = 5,316 cells), DSB (n = 725 cells).

(B) Full chromosome (chr8) Hi-C chromatin interaction heatmaps.

(C) Differential heatmaps comparing Step 1/Control and Step 2/Control, colored by increased (red) or decreased (blue) interactions over control.

(D) Representative Hi-C interaction plots showing the disruption of TADs. Hi-C heatmaps were rotated 45°, and only the upper triangle is shown.

(E) Quantification of TAD disruption through inclusion ratio (IR). IR is the ratio of intra-TAD interactions to outside-TAD interactions (Wilcoxon test with BH correction).

(F) Representative Hi-C interaction plots showing the disruption of chromatin loops.

(G) Aggregate heatmaps of reduced intensity (>2-fold), increased intensity (>2-fold), and conserved (<25% change) chromatin loops for Step 1 vs. Control and Step 2 vs. Control.

(H) Bar plot indicating quantification of chromatin loop disruption in Step 1 (red) and Step 2 (dark red).

(I) Aggregate plots of BLISS reads centered at loop anchors in CK-p25 neurons.

See also [Figure S4](#), [Table S1](#), pages 8–10 and 16.



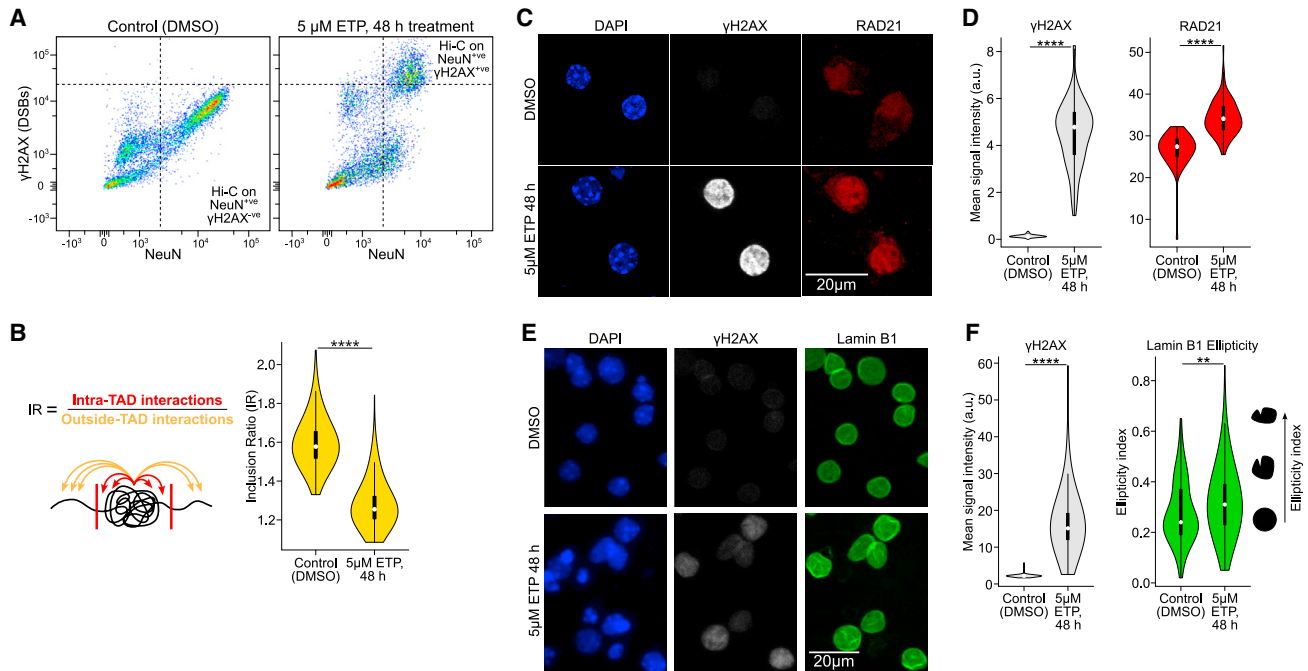


**Figure 4. DSBs in neurons are sufficient to disrupt the 3D genome organization**

(A) FANS dot-plots of NeuN versus  $\gamma$ H2AX immunoreactivity after etoposide (5  $\mu$ M for 48 h) or vehicle (DMSO) treatment in primary neuronal culture.

(B) Quantification of TAD disruption (IR, Wilcoxon test, \*\*\*\* $p < 1e-4$ ).

(C) Representative images and quantification of RAD21 (cohesin subunit) IHC in primary culture neurons (DIV 12) after etoposide (5  $\mu$ M for 48 h) or vehicle treatment (DMSO).

(D) Violin plots quantifying the images for  $\gamma$ H2AX levels (gray) and RAD21 levels (red) in control neurons and etoposide-treated neurons (Wilcoxon test). The mean relative intensity of  $\gamma$ H2AX and RAD21 was measured within NeuN surfaces. Control (n = 111 cells), ETP (n = 112 cells).

(E) Representative images of Lamin B1 IHC in primary culture neurons (DIV 12) after etoposide (5  $\mu$ M for 48 h) or vehicle treatment (DMSO).

(F) Violin plots quantifying the images for  $\gamma$ H2AX levels (red) and lamin B1 ellipticity (green) in control neurons and etoposide-treated neurons (Wilcoxon test, \*\* $p < 0.01$ , \*\*\*\* $p < 1e-4$ ). The mean relative intensity of  $\gamma$ H2AX was measured within lamin B1 surfaces that were positive for NeuN. Control (n = 78), ETP (n = 809). See also Figure S5, Table S1, page 11 and 16.

in T-cells and B-cells.<sup>28</sup> The enrichment of DSBs at loop boundaries was lowest in Step 1, followed by Step 2, which is consistent with the stochastic increase in DSB burden in Step 1 and partial repair in Step 2 (Figures 3I and S3B).

### Induction of DSBs in neurons is sufficient to disrupt the 3D genome organization

Next, we sought to test if the induction of DSBs by an alternate mechanism independent of the CK-p25 model would recapitulate the DSB-mediated effects on the 3D genome organization. We observed increased genome structural variations in cultured primary neurons where persistent DSBs were induced by etoposide treatment (Figure 1J). Therefore, we wondered if the induction of DSBs by etoposide would also elicit changes in the 3D genome organization. To test this, we treated primary mouse cortical neurons with either 5  $\mu$ M etoposide for 48 h or DMSO. We FANS sorted NeuN<sup>+</sup> neurons with high  $\gamma$ H2AX from the etoposide treatment and NeuN<sup>+</sup> neurons with baseline  $\gamma$ H2AX from the DMSO treatment (Figure 4A). Next, we performed *in situ* Hi-C, but at a lower read depth. We observed a reduction in TAD integrity and loop intensities similar to CK-p25 (Figure S5A). Quantifying TAD integrity using inclusion ratio revealed a significant reduction in the etoposide-treated primary neuronal cultures similar to that of *in vivo* neu-

rons from CK-p25 mice with high DSB burden (Figure 4B; Table S1, page 11). The level of induction of DSBs, as measured by  $\gamma$ H2AX levels in FANS, was dependent on etoposide concentration (Figure S5B), and treating primary neurons with a lower concentration of etoposide (1  $\mu$ M, 48 h) also produced a significant reduction in the inclusion ratio (Figure S5C).

CK-p25 neurons burdened with DSBs exhibited disruption of RAD21 and Lamin B1, two structural proteins involved in DSB repair and 3D genome organization (Figures 3A and S4A–S4D). To measure the effect of etoposide-induced DSBs on levels of cohesin, we stained for RAD21 in primary cortical neurons treated with 5  $\mu$ M etoposide for 48 h compared to DMSO-treated control. Like CK-p25 neurons with high DSB burden, RAD21 levels were significantly elevated in neurons harboring etoposide-mediated DSBs (Figures 4C and 4D). Next, we stained for Lamin B1 in primary neurons treated with etoposide and observed the disruption of Lamin B1 at the nuclear envelope similar to the CK-p25 mouse model (Figures 4E, 4F, and S4D). Etoposide-treated neurons also showed increased senescence-like and immune gene expression signatures indicating the similar molecular mechanisms underlying the disruption of genome organization and stability between etoposide-treated neurons and the CK-p25 mouse model (Figure S5D).

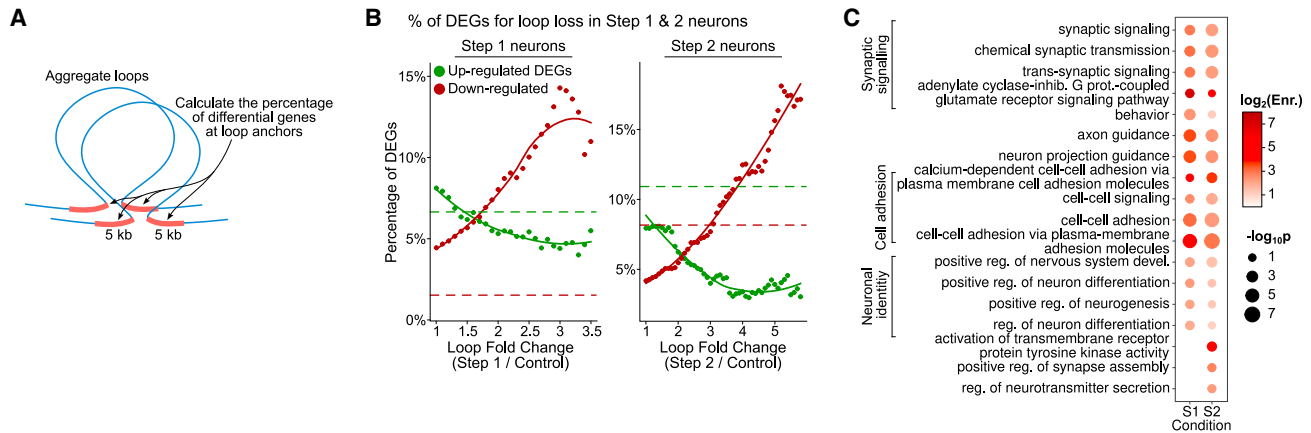


**Figure 5. DSB-associated dysregulation of the 3D genome aligns with the differential gene expression**

(A) Schematic for comparison of differential loops to differential gene expression in neurons with DSBs. Differential loops were identified for increasing fold change thresholds of loop score. For each differential loop, genes within  $\pm 5$  kb of the loop base were identified and the percentage of differentially expressed genes (DEGs) was calculated. Percentage DEGs were then plotted against the thresholds used for calling the differential loops. (B) Percentage of up (green) and down (red) DEGs vs. loop fold change for loop loss in both Step 1 and 2. Red and green dotted lines are the baseline percentage of up and down DEGs genome-wide, respectively. (C) Gene ontology analysis (GORILLA) of loop loss-associated down-regulated genes. See also [Figure S6](#), [Table S1](#), page 10, 14, and 16.

To further explore the association between DSBs and the 3D genome disruption in neurons, we turned to the Tau P301S model of tauopathy, an additional mouse model of neurodegeneration.<sup>92</sup> While not as pronounced as the CK-p25 model, where a distinct subset of neurons harbors high levels of DSBs, neurons in Tau P301S mice show a pan-neuronal increase in DSBs.<sup>93</sup> We performed *in situ* Hi-C on FANS-sorted NeuN<sup>+ve</sup> neuronal nuclei from the Tau P301S forebrain and WT littermates. Consistent with the observations in CK-p25 mice and etoposide-treated neurons, Hi-C in P301S neurons showed a decreased number of chromatin loops and a significant decrease in TAD integrity as measured by inclusion ratio ([Figures S5E and S5F](#); [Table S1](#), pages 12, 13). Together, these results demonstrate that DSBs in neurons are sufficient to disrupt the 3D genome organization.

### Disruption of the 3D genome organization by DSBs is associated with differential gene regulation

The 3D genome plays an important role in neuronal gene expression and function.<sup>36,37–40,94,95</sup> Chromatin loops enable interactions between enhancers and promoters enabling fine control of gene expression, in addition to the regulation mediated by transcription factors and other epigenetic modifications.<sup>27,96</sup> To investigate if the chromatin loop dysregulation in Step 1 and Step 2 neurons is associated with gene expression changes, we stratified differential loops at increasing fold-change thresholds and calculated the percentage of differential up and down-regulated genes (fold-change  $>2$ ,  $p$  value  $< 0.05$ ) near these loops ( $\pm 5$  kb from anchors) using bulk RNA-seq from Control, Step 1, and Step 2 neurons ([Figure 5A](#)).<sup>58</sup> Reduction in loop intensity was strongly associated with higher percentages of down-regulated genes in both Step 1 and Step 2 neurons and with lower percentages of up-regulated genes ([Figure 5B](#)). Down-regulated genes associated with loop loss were significantly enriched for synaptic,

cell adhesion, and neuronal development genes ([Figure 5C](#); [Table S1](#), page 14). On the other hand, loops with increased intensity did not have a consistent relationship with differential gene expression, suggesting that the association between loop gain and gene expression is context dependent ([Figure S6A](#)).<sup>97</sup>

Among the differential genes in Step 1 and Step 2 neurons, we found that cohesin complex genes were up-regulated alongside several previously reported DNA damage, senescence, and immune response genes ([Figure 6A](#)).<sup>58</sup> Cohesin complex genes were consistently and significantly up-regulated in excitatory neurons from subjects with high AD pathology in the 10x snRNA-seq data across 427 individuals ([Figure 6B](#)).<sup>60</sup> The increase in cohesin complex gene expression is also consistent with the increased levels of RAD21 in both CK-p25 neurons and etoposide-treated primary neuronal cultures ([Figures 3A and 4C](#)). Finally, we used immunohistochemistry to measure the levels of cohesin subunit RAD21 in human postmortem tissue and found significantly increased levels of RAD21 in neurons from subjects with AD pathology ([Figures 6C and 6D](#)).

Interestingly, we noticed histone genes were progressively up-regulated in Step 1 and Step 2 neurons ([Figure 6A](#)). Their differential changes were significantly correlated with increased histone gene expression in etoposide-treated primary neuronal cultures, suggesting that DSBs play a key role in their dysregulation ([Figure S6B](#)). To measure the regulation of histone genes in human AD pathology, we leveraged snRNA-seq across 427 individuals from Mathys et al.<sup>60</sup> Indeed, we found that several histones were upregulated in human AD in excitatory neurons along with the upregulation of the cohesin complex genes ([Figure 6B](#)). Strikingly, the strongly up-regulated histone genes included *H2AFX*, which encodes the histone H2AX, whose phosphorylation marks DSBs. Another up-regulated histone gene, *H2AFV*, codes for H2A.Z, whose increase is associated with persistent DNA damage, brain aging, and is negatively associated with

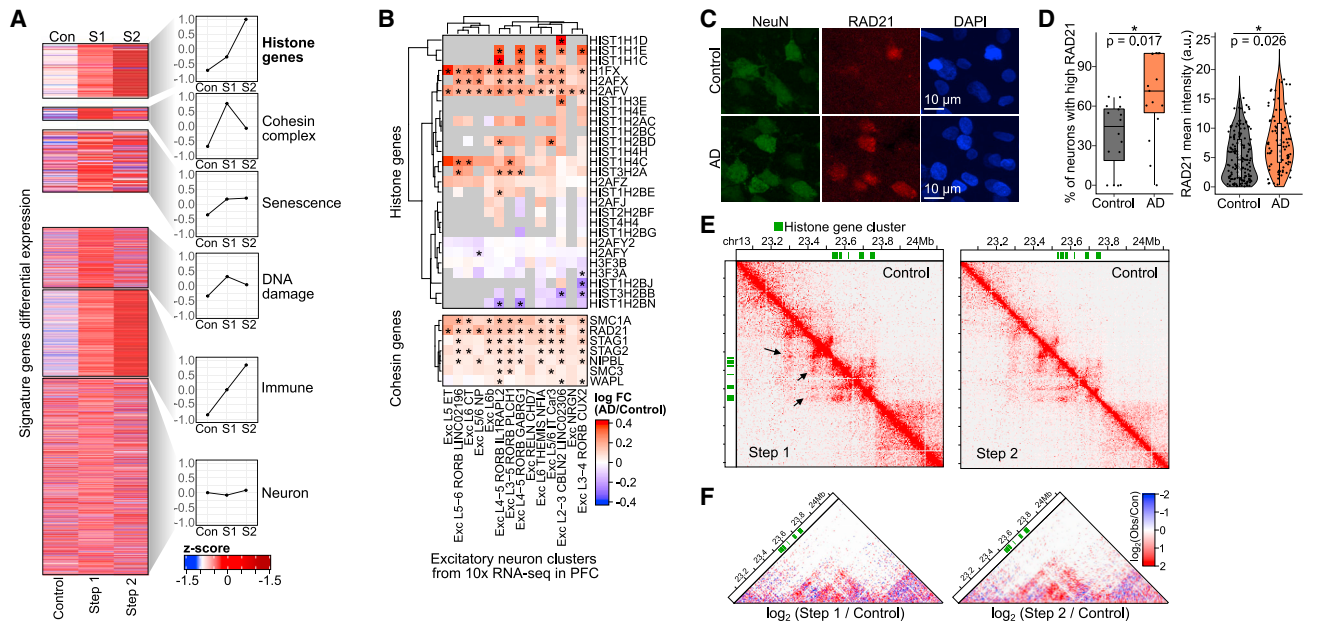


**Figure 6. Up-regulation of cohesin and histone genes in Alzheimer's disease**

(A) Heatmap of differential gene expression as Z scores from bulk RNA-seq in Control, Step 1, and Step 2 for signature gene sets. The right panels show average values for each set.  
 (B) Heatmap of differential expression of histone and cohesin genes across excitatory subtypes in 10x snRNA-seq from Mathys et al. (\*differential).<sup>60</sup>  
 (C) Representative immunostaining images of RAD21 in AD and Control human postmortem tissue.  
 (D) RAD21 staining was quantified as the percentage of neurons with high RAD21 (mean intensity >50th percentile) per image (left) or using RAD21 mean intensity (right). Significance was calculated using a linear mixed-model approach across AD 3 and 3 Control individuals (Table S1, page 15).  
 (E) Hi-C interaction matrix for histone gene cluster (green blocks, chr13). The lower diagonal is Step 1 or 2, upper is Control.  
 (F) Differential Hi-C heatmaps comparing Step 1/Control and Step 2/Control, colored by increased (red) or decreased (blue) interactions over control. Hi-C heatmaps were rotated 45° and only the upper triangle is shown.  
 See also Figure S6 and Table S1, page 5, 15, and 16.

memory formation.<sup>98–100</sup> A large number of histone genes are located as clusters in a 1 Mb region on mouse chromosome 13.<sup>101</sup> Remarkably, along with the increased gene expression of histone genes, the histone gene clusters on chromosome 13 gained *de novo* loops in Step 1 and Step 2 neurons (Figures 6E, 6F, S6C, and S6D). This highlights the 3D genome level regulation underlying the upregulation of histone gene clusters. Together, these results demonstrate the association between DSB-mediated 3D genome changes and gene regulation programs underlying neurodegeneration.

## DISCUSSION

Neurons' long lifespan and the lack of sister chromatids for homologous recombination repair leave them vulnerable to DSBs.<sup>102</sup> Recent studies have shown neuronal activity-dependent DSBs and associated repair mechanisms.<sup>9,11,103</sup> In addition, extensive neuronal activity-induced demethylation could be a source of DNA single-stranded breaks through the Tet-TDG pathway-mediated base excision repair.<sup>12,13</sup> Recent studies have discovered a non-random distribution of DNA damage in the neuronal genome,<sup>104</sup> notably, neuronal enhancers as hotspots of single-stranded breaks, presumably through multiple cycles of enhancer cytosine methylation and demethylation.<sup>8,10</sup> These processes compound the

vulnerability of neurons to DNA damage compared to other brain cell types.

Neurons start accumulating DSBs early in the progression of AD.<sup>2,4–7</sup> We found a significant association between the expression of DNA repair pathway genes and AD pathology in single-nucleus profiling of AD brains (Mathys et al. in this issue).<sup>60</sup> In addition, mutations in DNA repair pathway components lead to neurodevelopment and neurodegenerative diseases.<sup>105,106</sup> Interestingly, we found a modest but not significant enrichment of protein-coding genes related to DNA damage repair in the published AD GWAS catalog (NHGRI-EBI, OR = 1.22, 62 GWAS/DNA damage repair genes),<sup>75</sup> including crucial DSB repair genes such as *ATM*, *HMG2*, and *EXO1*. This apparent lack of statistical significance may be because certain mutations in DNA repair genes predispose individuals to premature death before AD onset through accelerated aging and other severe diseases such as cancer and diabetes, leading to their underrepresentation in GWAS.<sup>107,108</sup> Consistent with this hypothesis, DNA damage repair pathways were found to be significantly enriched in Huntington's disease GWAS analysis, a neurodegenerative disease with a much earlier age of disease onset.<sup>109</sup>

DSBs are repaired via the classical non-homologous end-joining (NHEJ) pathway in post-mitotic cells and can lead to genome structural variations.<sup>17–20</sup> Further, genome structural

variations can lead to gene fusions and are often drivers of cancer,<sup>110</sup> and are detectable from bulk RNA-seq.<sup>59,111–113</sup> Gene fusions are an attractive proxy for comparing the rate of genome structural variations in AD and non-AD individuals using single-cell RNA-seq, but detection and validation of independent mosaic fusions or structural variations in single cells remain challenging in the absence of clonality.<sup>114–118</sup> Instead, in this study we report an increased burden of mosaic gene fusions in excitatory neurons in individuals with AD pathology by calling fusion events in single-cell RNA-seq in human postmortem samples in each cell independently. Gene fusions are also particularly enriched in excitatory neurons with DNA damage, senescence, and cohesin gene signatures. Indeed, accumulation of DNA damage can lead to a senescence-like state in neurons and has been implicated in the progression of AD.<sup>119–121</sup>

In the CK-p25 model of neurodegeneration, neurons progress through an initial step with increased DSBs (Step 1) to a later step enriched for gene fusions and structural variation and marked by senescence genes (Step 2).<sup>58</sup> We hypothesize that persistent DSBs in neurons lead to genome structural variations, consistent with DSB induction by etoposide, where persistent but not acute DSB induction leads to increased structural variations. Gene fusion junctions were enriched for DSBs and fusions were enriched for genes with higher expression and length, consistent with previous observations in non-neuronal cells and neural precursor cells.<sup>68,73</sup> Surprisingly, Step 1 showed lower DSB enrichments for highly transcribed and long genes, and DSBs were supported by fewer UMIs, suggesting that Step 1 DSBs are largely stochastic. By contrast, UMIs in Step 2 were distributed similarly to controls, suggesting increased repair of DSBs at the price of structural variations. We propose that the increased stochastic DSB burden strains the DNA repair resources, leading to defective DNA repair and genome structural variations that disproportionately affect hotspots of DNA breaks such as highly expressed genes, long genes, and loop anchors. Future studies that map DSBs directly in postmortem tissue could reveal additional hotspots associated with structural variations in AD.

Previous studies have shown increased neuronal genomic mosaicism (including SNVs, copy number variations, and cDNA insertions in neurodegeneration).<sup>122–126</sup> Recently, a study identified an increase in mosaicism due to recombination between Alu and L1 elements in Parkinson's and Alzheimer's disease.<sup>118</sup> Here we report gene fusions and genome structural variations mediated by DSBs in neurons as a class of mosaic somatic genomic change exacerbated in neurodegeneration. Genome structural variations can bring ectopic regulatory elements next to genes causing pathological up- or down-regulation of genes. Interestingly, genome structural variations have been shown to cause pathological TAD fusions and create neo-TADs in several cancers. For instance, a neo-TAD caused by structural variation was associated with higher expression of the oncogene MYC in neuroblastomas.<sup>23</sup> Therefore, it's likely that structural variations in neurons could impact the expression of important neuronal genes in AD. Gene fusions at important neural genes can result in a pathological gain or loss of their function and result in defects in neuronal function. Indeed, we find that long-neural genes with synaptic and cell adhesion genes

associated with the recurrent DNA double-strand breaks and AD GWAS genes are enriched for gene fusions.<sup>73</sup> We also demonstrate a link between genome structural variations and the senescence-like state in neurons. Indeed, genomic mosaicism by retro transposition of LINE-1 elements has been associated with the neuronal genome and the derepression of LINE-1 elements has been associated with senescence.<sup>127–129</sup> These observations combined with our results suggest that genomic mosaicism is an important driver of senescence in neurons and could contribute to the pathogenesis of neurodegenerative disease.

In addition to the disruptions in the linear genome, we show that the DSB-mediated senescence-like state in neurons leads to the disruption of the 3D genome in neurodegeneration. We observed a general loss of TAD definition and loop intensities, especially in Step 2 senescence-like neurons along with differential regulation of several genes associated with neuronal identity. This is strikingly similar to epigenome erosion, particularly in excitatory neurons and oligodendrocytes, characterized by the loss of cell-type-specific chromatin accessibility profile reported in the companion manuscript.<sup>87</sup> Interestingly, erosion of epigenetic information, TAD insulation, and cell identity was recently reported in a mouse model with inducible DNA damage (ICE mouse model) accompanied by brain aging and cognitive decline.<sup>130</sup> A recent study proposed that DSBs can act as roadblocks to loop extrusion.<sup>32</sup> It's conceivable that adjacent DSBs may cause premature loop extrusion block on both sides, thereby disrupting chromatin loops and larger domains. Surprisingly, X-ray radiation-induced DSBs increased the segregation of TADs in fibroblasts.<sup>54</sup> Future studies should explore how acute DSBs formed by irradiation vs. persistent DSBs impact genome organization and additionally how post-mitotic cells and dividing cells differ in their response to DSBs. We also observed DSB-mediated changes in the levels of nuclear structural proteins, cohesin, and Lamin B1, in neurons enriched for DSBs, similar to previous observations in AD neurons and also in senescent astrocytes.<sup>131,132</sup> Despite the disruption of lamin B1, the A/B compartmentalization of the genome remained relatively unaffected, which is in concordance with the observations in retinal rod neurons, where despite the loss of heterochromatin interactions with the nuclear lamina, phase separation drives the formation of A/B compartments.<sup>133</sup>

Changes in the 3D genome aligned with transcriptional changes overall, with reduced loop intensities having a striking correlation with the down-regulation of genes. Interestingly, we observed the *de-novo* establishment of loops at histone gene clusters that aligned with the upregulation of several histone genes. Previous studies have shown the importance of histones in DNA damage response, senescence, brain aging, neuronal identity, and memory formation.<sup>98–100,134–137</sup> These results highlight a link between the 3D genome organization in neurons and transcriptional programs associated with the neurodegenerative state. Indeed, while the gain of chromatin loops is associated with histone gene up-regulation, other independent mechanisms of gene regulation may underlie the up-regulation of genes in degenerating neurons. Additionally, studies have shown senescence-associated 3D genome reorganization in dividing cell types.<sup>42,138–141</sup> Our results show



that the 3D genome organization changes in neurons in a senescence-like state may mediate genome dysfunction in neurodegeneration.

Overall, our work demonstrates that DNA double-strand breaks lead to mosaic genome structural variations and the disruption of 3D genome organization in neurons. We observe increased mosaic gene fusions caused by genome structural variations in excitatory neurons associated with increased cohesin, DNA damage, and senescence-like gene expression in Alzheimer's disease. These data link neuronal genomic integrity and 3D genome organization to cellular pathologies underlying neurodegeneration.

### Limitations of the study

Gene fusions arise from a subset of genome structural variations, and future technologies coupling single-cell RNA sequencing with long-read single-cell genome sequencing will be required to resolve the full extent of DNA damage-dependent genome structural variations in neurodegeneration. Single-cell RNA-seq provides a sparse readout of gene expression and is likely to generally underestimate the number of gene fusions in each cell. While relatively uncommon, chimeric molecules arising through PCR artifacts and random ligations during library preparation are difficult to distinguish from chimeric molecules arising from true mosaic gene fusions. We make the assumption that AD vs. Control classification and various gene expression pattern enrichments explored in this do not modify PCR artifacts and random ligations during library preparation. The disruption in the 3D genome organization could be caused both directly by unresolved DSBs and by genome structural variations. In the current study, we are unable to resolve the precise role of each of these components. Future studies that perform targeted Hi-C at unresolved DSBs locations vs. post-repair locations will be better positioned to answer these questions.

### STAR★METHODS

Detailed methods are provided in the online version of this paper and include the following:

- **KEY RESOURCES TABLE**
- **RESOURCE AVAILABILITY**
  - Lead contact
  - Materials availability
  - Data and code availability
- **EXPERIMENTAL MODEL AND STUDY PARTICIPANT DETAILS**
  - Human subjects
  - Animal models
  - Primary neuron culture
  - MADRC brain tissue samples
- **METHOD DETAILS**
  - Single-nucleus Smart-seq2
  - Oxford nanopore Technology (ONT) sequencing and analysis
  - Fluorescence-activated nuclei sorting
  - *In situ* Hi-C

- Break-Labeling *in situ* and sequencing (BLISS)
- Mate-pair sequencing
- Immunofluorescence microscopy
- **QUANTIFICATION AND STATISTICAL ANALYSIS**
  - Smart-seq2 cell identities
  - Gene fusions calling
  - Gene fusions quantification
  - Mate-pair seq analysis
  - BLISS data analysis
  - Oxford nanopore Technology (ONT) sequencing analysis
  - Hi-C analysis
  - Gene ontology analysis
  - Human RAD21 staining analysis
- **ADDITIONAL RESOURCES**

### SUPPLEMENTAL INFORMATION

Supplemental information can be found online at <https://doi.org/10.1016/j.cell.2023.08.038>.

### ACKNOWLEDGMENTS

This work was supported in part by NIH grants NS102730, NS051874, AG054012, Cure Alzheimer's Fund, JPB Foundation, and the Glenn Foundation for Aging Research to L.-H.T. NIH U01 NS110453 and NIH R01 AG058002 for M.K. and L.-H.T. V.D. was supported by NIH Pathway to Independence Award K99 AG073466 and Alzheimer's Association fellowship AARF-19-618751. C.A.B. was supported by NIH training grant GM087237. H.M. was supported by an Early Postdoc Mobility fellowship from the Swiss National Science Foundation (P2BSP3\_151885). ROSMAP is supported by P30AG10161, P30AG72975, R01AG15819, R01AG17917. U01AG46152, U01AG61356 to D.A.B. ROSMAP resources can be requested at <https://www.radc.rush.edu>. We thank Dr. Ping-Chieh Pao, Dr. Jay Penny, Dr. Mathew Victor, Dr. William Ravenius, the members of Tsai Lab, Dr. Maria Kousi, the members of Kellis Lab, and Dr. Vladimir Seplyarskiy for all the constructive discussions and feedback on the manuscript. We would also like to thank Ying Zhou and Erica McNamara of the Tsai Lab, Glenn Paradis and the team at Koch Institute Flow Cytometry Core, as well as Dr. Stuart Levine and the team at the MIT BioMicro Center.

### AUTHOR CONTRIBUTIONS

V.D. and L.-H.T. conceptualized and designed the project. V.D. performed and analyzed the Hi-C, BLISS, and mate-pair sequencing in CK-p25 and primary culture neurons. V.D. performed the tissue preparation and FACS sorting. C.A.B. performed the majority of the Smart-seq2, 10x RNA-seq, and ONT sequencing data analysis for gene fusions along with V.D. V.D. prepared Oxford nanopore libraries, and C.A.B. and V.D. analyzed the long read sequencing data. H.M. and Z.P. performed the human Smart-seq2 library preparation. V.D. and A.M. performed the P301S mice Hi-C library preparation. A.M., V.D., A.L., and R.J. performed immunostaining, imaging, and analysis. G.M.W. and H.S.M. helped with experimental design and setup. D.A.B. provided the human postmortem samples. V.D., C.A.B., M.K., and L.-H.T. wrote and revised the manuscript with input from all authors. L.-H.T. and M.K. provided the resources for the project.

### DECLARATION OF INTERESTS

L.-H.T. is a member of the Scientific Advisory Board of Cognito Therapeutics, 4M Therapeutics, Cell Signaling Technology, and Souvien Therapeutics, which has no association to the work described in this manuscript.

## INCLUSION AND DIVERSITY

We support inclusive, diverse, and equitable conduct of research.

Received: September 22, 2022

Revised: April 2, 2023

Accepted: August 29, 2023

Published: September 28, 2023

## REFERENCES

- Lu, T., Pan, Y., Kao, S.Y., Li, C., Kohane, I., Chan, J., and Yankner, B.A. (2004). Gene regulation and DNA damage in the ageing human brain. *Nature* 429, 883–891. <https://doi.org/10.1038/nature02661>.
- Madabhushi, R., Pan, L., and Tsai, L.H. (2014). DNA damage and its links to neurodegeneration. *Neuron* 83, 266–282. <https://doi.org/10.1016/j.neuron.2014.06.034>.
- Provasek, V.E., Mitra, J., Malojirao, V.H., and Hegde, M.L. (2022). DNA Double-Strand Breaks as Pathogenic Lesions in Neurological Disorders. *Int. J. Mol. Sci.* 23, 4653. <https://doi.org/10.3390/ijms23094653>.
- Adamec, E., Vonsattel, J.P., and Nixon, R.A. (1999). DNA strand breaks in Alzheimer's disease. *Brain Res.* 849, 67–77. [https://doi.org/10.1016/S0006-8993\(99\)02004-1](https://doi.org/10.1016/S0006-8993(99)02004-1).
- Thadathil, N., Delotterie, D.F., Xiao, J., Hori, R., McDonald, M.P., and Khan, M.M. (2021). DNA Double-Strand Break Accumulation in Alzheimer's Disease: Evidence from Experimental Models and Postmortem Human Brains. *Mol. Neurobiol.* 58, 118–131. <https://doi.org/10.1007/s12035-020-02109-8>.
- Shanbhag, N.M., Evans, M.D., Mao, W., Nana, A.L., Seeley, W.W., Adame, A., Rissman, R.A., Masliah, E., and Mucke, L. (2019). Early neuronal accumulation of DNA double strand breaks in Alzheimer's disease. *Acta Neuropathol. Commun.* 7, 77–18. <https://doi.org/10.1186/s40478-019-0723-5>.
- Tse, K.H., Cheng, A., Ma, F., and Herrup, K. (2018). DNA damage-associated oligodendrocyte degeneration precedes amyloid pathology and contributes to Alzheimer's disease and dementia. *Alzheimer's Dement.* 14, 664–679. <https://doi.org/10.1016/j.jalz.2017.11.010>.
- Wu, W., Hill, S.E., Nathan, W.J., Paiano, J., Callen, E., Wang, D., Shinoda, K., van Wietmarschen, N., Colón-Mercado, J.M., Zong, D., et al. (2021). Neuronal enhancers are hotspots for DNA single-strand break repair. *Nature* 593, 440–444. <https://doi.org/10.1038/s41586-021-03468-5>.
- Madabhushi, R., Gao, F., Pfenning, A.R., Pan, L., Yamakawa, S., Seo, J., Rueda, R., Phan, T.X., Yamakawa, H., Pao, P.-C., et al. (2015). Activity-Induced DNA Breaks Govern the Expression of Neuronal Early-Response Genes. *Cell* 161, 1592–1605. <https://doi.org/10.1016/j.cell.2015.05.032>.
- Reid, D.A., Reed, P.J., Schlachetzki, J.C.M., Nituлесcu, I.I., Chou, G., Tsui, E.C., Jones, J.R., Chandran, S., Lu, A.T., McClain, C.A., et al. (2021). Incorporation of a nucleoside analog maps genome repair sites in postmitotic human neurons. *Science* 372, 91–94. <https://doi.org/10.1126/science.abb9032>.
- Suberbielle, E., Sanchez, P.E., Kravitz, A.V., Wang, X., Ho, K., Eilertson, K., Devidze, N., Kreitzer, A.C., and Mucke, L. (2013). Physiologic brain activity causes DNA double-strand breaks in neurons, with exacerbation by amyloid- $\beta$ . *Nat. Neurosci.* 16, 613–621. <https://doi.org/10.1038/nn.3356>.
- Guo, J.U., Ma, D.K., Mo, H., Ball, M.P., Jang, M.H., Bonaguidi, M.A., Balazer, J.A., Eaves, H.L., Xie, B., Ford, E., et al. (2011). Neuronal activity modifies the DNA methylation landscape in the adult brain. *Nat. Neurosci.* 14, 1345–1351. <https://doi.org/10.1038/NN.2900>.
- DeNizio, J.E., Dow, B.J., Serrano, J.C., Ghanty, U., Drohat, A.C., and Kohli, R.M. (2021). TET-TDG active DNA demethylation at CpG and non-CpG sites. *J. Mol. Biol.* 433, 166877. <https://doi.org/10.1016/j.JMB.2021.166877>.
- Yu, H., Harrison, F.E., and Xia, F. (2018). Altered DNA repair; An early pathogenic pathway in Alzheimer's disease and obesity. *Sci. Rep.* 8, 5600. <https://doi.org/10.1038/s41598-018-23644-4>.
- Suberbielle, E., Djukic, B., Evans, M., Kim, D.H., Taneja, P., Wang, X., Finucane, M., Knox, J., Ho, K., Devidze, N., et al. (2015). DNA repair factor BRCA1 depletion occurs in Alzheimer brains and impairs cognitive function in mice. *Nat. Commun.* 6, 8897. <https://doi.org/10.1038/ncomms9897>.
- Aguilera, A., and García-Muse, T. (2013). Causes of genome instability. *Annu. Rev. Genet.* 47, 1–32. <https://doi.org/10.1146/annurev-genet-111212-133232>.
- Iyama, T., and Wilson, D.M. (2013). DNA repair mechanisms in dividing and non-dividing cells. *DNA Repair* 12, 620–636. <https://doi.org/10.1016/j.DNAREP.2013.04.015>.
- Richardson, C., and Jasin, M. (2000). Frequent chromosomal translocations induced by DNA double-strand breaks. *Nature* 405, 697–700. <https://doi.org/10.1038/35015097>.
- Ferguson, D.O., and Alt, F.W. (2001). DNA double strand break repair and chromosomal translocation: Lessons from animal models. *Oncogene* 20, 5572–5579. <https://doi.org/10.1038/sj.onc.1204767>.
- Lin, C., Yang, L., Tanasa, B., Hutt, K., Ju, B.g., Ohgi, K., Zhang, J., Rose, D.W., Fu, X.D., Glass, C.K., and Rosenfeld, M.G. (2009). Nuclear Receptor-Induced Chromosomal Proximity and DNA Breaks Underlie Specific Translocations in Cancer. *Cell* 139, 1069–1083. <https://doi.org/10.1016/j.cell.2009.11.030>.
- Rabbitts, T.H. (1994). Chromosomal translocations in human cancer. *Nat* 372, 143–149. <https://doi.org/10.1038/372143a0>.
- Li, Y., Roberts, N.D., Wala, J.A., Shapira, O., Schumacher, S.E., Kumar, K., Khurana, E., Waszak, S., Korbel, J.O., Haber, J.E., et al. (2020). Patterns of somatic structural variation in human cancer genomes. *Nature* 578, 112–121. <https://doi.org/10.1038/s41586-019-1913-9>.
- Dixon, J.R., Xu, J., Dileep, V., Zhan, Y., Song, F., Le, V.T., Yardımcı, G.G., Chakraborty, A., Bann, D.V., Wang, Y., et al. (2018). Integrative detection and analysis of structural variation in cancer genomes. *Nat. Genet.* 50, 1388–1398. <https://doi.org/10.1038/s41588-018-0195-8>.
- Xu, J., Song, F., Lyu, H., Kobayashi, M., Zhang, B., Zhao, Z., Hou, Y., Wang, X., Luan, Y., Jia, B., et al. (2022). Subtype-specific 3D genome alteration in acute myeloid leukaemia. *Nature* 611, 387–398. <https://doi.org/10.1038/s41586-022-05365-x>.
- Botten, G.A., Zhang, Y., Dudnyk, K., Kim, Y.J., Liu, X., Sanders, J.T., Imanci, A., Droin, N., Cao, H., Kaple, P., et al. (2023). Structural variation cooperates with permissive chromatin to control enhancer hijacking-mediated oncogenic transcription. *Blood* 142, 336–351. <https://doi.org/10.1182/blood.2022017555>.
- Caldecott, K.W., Ward, M.E., and Nussenzweig, A. (2022). The threat of programmed DNA damage to neuronal genome integrity and plasticity. *Nat. Genet.* 54, 115–120. <https://doi.org/10.1038/s41588-021-01001-y>.
- Schoenfelder, S., and Fraser, P. (2019). Long-range enhancer–promoter contacts in gene expression control. *Nat. Rev. Genet.* 20, 437–455. <https://doi.org/10.1038/s41576-019-0128-0>.
- Canela, A., Maman, Y., Jung, S., Wong, N., Callen, E., Day, A., Kieffer-Kwon, K.-R., Pekowska, A., Zhang, H., Rao, S.S.P., et al. (2017). Genome Organization Drives Chromosome Fragility. *Cell* 170, 507–521.e18. <https://doi.org/10.1016/j.cell.2017.06.034>.
- Zhang, H., Emerson, D.J., Gilgenast, T.G., Titus, K.R., Lan, Y., Huang, P., Zhang, D., Wang, H., Keller, C.A., Giardine, B., et al. (2019). Chromatin structure dynamics during the mitosis-to-G1 phase transition. *Nature* 576, 158–162. <https://doi.org/10.1038/s41586-019-1778-y>.
- Zhang, Y., McCord, R.P., Ho, Y.J., Lajoie, B.R., Hildebrand, D.G., Simon, A.C., Becker, M.S., Alt, F.W., and Dekker, J. (2012). Spatial organization of the mouse genome and its role in recurrent chromosomal translocations. *Cell* 148, 908–921. <https://doi.org/10.1016/j.cell.2012.02.002>.

31. Ba, Z., Lou, J., Ye, A.Y., Dai, H.Q., Dring, E.W., Lin, S.G., Jain, S., Kyritsis, N., Kieffer-Kwon, K.R., Casellas, R., and Alt, F.W. (2020). CTCF orchestrates long-range cohesin-driven V(D)J recombinational scanning. *Nature* 586, 305–310. <https://doi.org/10.1038/s41586-020-2578-0>.
32. Arnould, C., Rocher, V., Finoux, A.L., Clouaire, T., Li, K., Zhou, F., Caron, P., Mangeot, P.E., Ricci, E.P., Mourad, R., et al. (2021). Loop extrusion as a mechanism for formation of DNA damage repair foci. *Nature* 590, 660–665.
33. Gibcus, J.H., Samejima, K., Goloborodko, A., Samejima, I., Naumova, N., Nuebler, J., Kanemaki, M.T., Xie, L., Paulson, J.R., Earnshaw, W.C., et al. (2018). A pathway for mitotic chromosome formation. *Science* 359, eaao6135. <https://doi.org/10.1126/science.aao6135>.
34. Dileep, V., Ay, F., Sima, J., Vera, D.L., Noble, W.S., and Gilbert, D.M. (2015). Topologically associating domains and their long-range contacts are established during early G1 coincident with the establishment of the replication-timing program. *Genome Res.* 25, 1104–1113. <https://doi.org/10.1101/gr.183699.114>.
35. Sima, J., Chakraborty, A., Dileep, V., Michalski, M., Klein, K.N., Holcomb, N.P., Turner, J.L., Paulsen, M.T., Rivera-Mulia, J.C., Trevilla-Garcia, C., et al. (2019). Identifying cis Elements for Spatiotemporal Control of Mammalian DNA Replication. *Cell* 176, 816–830.e18. <https://doi.org/10.1016/j.cell.2018.11.036>.
36. Yamada, T., Yang, Y., Valnegri, P., Juric, I., Abnoui, A., Markwalter, K.H., Guthrie, A.N., Godec, A., Oldenborg, A., Hu, M., et al. (2019). Sensory experience remodels genome architecture in neural circuit to drive motor learning. *Nature* 569, 708–713. <https://doi.org/10.1038/s41586-019-1190-7>.
37. Fernandez-Albert, J., Lipinski, M., Lopez-Cascales, M.T., Rowley, M.J., Martin-Gonzalez, A.M., del Blanco, B., Corces, V.G., and Barco, A. (2019). Immediate and deferred epigenomic signatures of in vivo neuronal activation in mouse hippocampus. *Nat. Neurosci.* 22, 1718–1730. <https://doi.org/10.1038/s41593-019-0476-2>.
38. Beagan, J.A., Pastuzyn, E.D., Fernandez, L.R., Guo, M.H., Feng, K., Titus, K.R., Chandrashekar, H., Shepherd, J.D., and Phillips-Cremins, J.E. (2020). Three-dimensional genome restructuring across timescales of activity-induced neuronal gene expression. *Nat. Neurosci.* 23, 707–717. <https://doi.org/10.1038/s41593-020-0634-6>.
39. Marco, A., Meharena, H.S., Dileep, V., Raju, R.M., Davila-Velderrain, J., Zhang, A.L., Adaikkan, C., Young, J.Z., Gao, F., Kellis, M., and Tsai, L.H. (2020). Mapping the epigenomic and transcriptomic interplay during memory formation and recall in the hippocampal engram ensemble. *Nat. Neurosci.* 23, 1606–1617. <https://doi.org/10.1038/s41593-020-00717-0>.
40. Dileep, V., and Tsai, L.H. (2021). Three-dimensional chromatin organization in brain function and dysfunction. *Curr. Opin. Neurobiol.* 69, 214–221. <https://doi.org/10.1016/J.CONB.2021.04.006>.
41. Marco, A. (2022). Activity-dependent remodeling of genome architecture in engram cells facilitates memory formation and recall. *Neural Regen. Res.* 17, 991–993. <https://doi.org/10.4103/1673-5374.324834>.
42. Meharena, H.S., Marco, A., Dileep, V., Lockshin, E.R., Akatsu, G.Y., Mullahoo, J., Watson, L.A., Ko, T., Guerin, L.N., Abdurrob, F., et al. (2022). Down-syndrome-induced senescence disrupts the nuclear architecture of neural progenitors. *Cell Stem Cell* 29, 116–130.e7. <https://doi.org/10.1016/J.STEM.2021.12.002>.
43. Sun, J.H., Zhou, L., Emerson, D.J., Phyto, S.A., Titus, K.R., Gong, W., Gilgenast, T.G., Beagan, J.A., Davidson, B.L., Tassone, F., and Phillips-Cremins, J.E. (2018). Disease-Associated Short Tandem Repeats Co-localize with Chromatin Domain Boundaries. *Cell* 175, 224–238.e15. <https://doi.org/10.1016/j.cell.2018.08.005>.
44. Lewis, P.N., Lukiw, W.J., De Boni, U., and McLachlan, D.R. (1981). Changes in Chromatin Structure Associated with Alzheimer's Disease. *J. Neurochem.* 37, 1193–1202. <https://doi.org/10.1111/j.1471-4159.1981.tb04670.x>.
45. Bendl, J., Hauberg, M.E., Girdhar, K., Im, E., Vicari, J.M., Rahman, S., Fernando, M.B., Townsley, K.G., Dong, P., Misir, R., et al. (2022). The three-dimensional landscape of cortical chromatin accessibility in Alzheimer's disease. *Nat. Neurosci.* 25, 1366–1378. <https://doi.org/10.1038/s41593-022-01166-7>.
46. Won, H., De La Torre-Ubieta, L., Stein, J.L., Parikshak, N.N., Huang, J., Opland, C.K., Gandal, M.J., Sutton, G.J., Hormozdiari, F., Lu, D., et al. (2016). Chromosome conformation elucidates regulatory relationships in developing human brain. *Nature* 538, 523–527. <https://doi.org/10.1038/nature19847>.
47. Rajarajan, P., Borrmann, T., Liao, W., Schrodde, N., Flaherty, E., Casiño, C., Powell, S., Yashaswini, C., LaMarca, E.A., Kassim, B., et al. (2018). Neuron-specific signatures in the chromosomal connectome associated with schizophrenia risk. *Science* 362, eaat4311. <https://doi.org/10.1126/science.aat4311>.
48. Nott, A., Holtman, I.R., Coufal, N.G., Schlachetzki, J.C.M., Yu, M., Hu, R., Han, C.Z., Pena, M., Xiao, J., Wu, Y., et al. (2019). Brain cell type-specific enhancer-promoter interactome maps and disease-risk association. *Science* 366, 1134–1139. <https://doi.org/10.1126/science.aay0793>.
49. Kikuchi, M., Hara, N., Hasegawa, M., Miyashita, A., Kuwano, R., Ikeuchi, T., and Nakaya, A. (2019). Enhancer variants associated with Alzheimer's disease affect gene expression via chromatin looping. *BMC Med. Genomics* 12, 128. <https://doi.org/10.1186/s12920-019-0574-8>.
50. Javierre, B.M., Burren, O.S., Wilder, S.P., Kreuzhuber, R., Várnai, C., Sewitz, S., Cairns, J., Wingett, S.W., Várnai, C., Thiecke, M.J., et al. (2016). Lineage-Specific Genome Architecture Links Enhancers and Non-coding Disease Variants to Target Gene Promoters. *Cell* 167, 1369–1384.e19. <https://doi.org/10.1016/j.cell.2016.09.037>.
51. Aymard, F., and Legube, G. (2016). A TAD closer to ATM. *Mol. Cell. Oncol.* 3, e1134411. <https://doi.org/10.1080/23723556.2015.1134411>.
52. Aymard, F., Aguirrebengoa, M., Guillou, E., Javierre, B.M., Bugler, B., Arnould, C., Rocher, V., Iacovoni, J.S., Biernacka, A., Skrzypczak, M., et al. (2017). Genome-wide mapping of long-range contacts unveils clustering of DNA double-strand breaks at damaged active genes. *Nat. Struct. Mol. Biol.* 24, 353–361. <https://doi.org/10.1038/nsmb.3387>.
53. Aten, J.A., Stap, J., Krawczyk, P.M., Van Oven, C.H., Hoebe, R.A., Essers, J., and Kanaar, R. (2004). Dynamics of DNA Double-Strand Breaks Revealed by Clustering of Damaged Chromosome Domains. *Science* 303, 92–95. <https://doi.org/10.1126/science.1088845>.
54. Sanders, J.T., Freeman, T.F., Xu, Y., Golloshi, R., Stallard, M.A., Hill, A.M., San Martin, R., Balajee, A.S., and McCord, R.P. (2020). Radiation-induced DNA damage and repair effects on 3D genome organization. *Nat. Commun.* 11, 6178. <https://doi.org/10.1038/s41467-020-20047-w>.
55. Wang, X., Luan, Y., and Yue, F. (2022). EagleC: A deep-learning framework for detecting a full range of structural variations from bulk and single-cell contact maps. *Sci. Adv.* 8, eabn9215. <https://doi.org/10.1126/sciadv.abn9215>.
56. Chakraborty, A., and Ay, F. (2018). Identification of copy number variations and translocations in cancer cells from Hi-C data. *Bioinformatics* 34, 338–345. <https://doi.org/10.1093/bioinformatics/btx664>.
57. Picelli, S., Faridani, O.R., Björklund, A.K., Winberg, G., Sagasser, S., and Sandberg, R. (2014). Full-length RNA-seq from single cells using Smart-seq2. *Nat. Protoc.* 9, 171–181. <https://doi.org/10.1038/nprot.2014.006>.
58. Welch, G.M., Boix, C.A., Schmauch, E., Davila-Velderrain, J., Victor, M.B., Dileep, V., Bozzelli, P.L., Su, Q., Cheng, J.D., Lee, A., et al. (2022). Neurons burdened by DNA double-strand breaks incite microglia activation through antiviral-like signaling in neurodegeneration. *Sci. Adv.* 8, eabo4662.
59. Haas, B.J., Dobin, A., Li, B., Stransky, N., Pochet, N., and Regev, A. (2019). Accuracy assessment of fusion transcript detection via read-mapping and de novo fusion transcript assembly-based methods. *Genome Biol.* 20, 213. <https://doi.org/10.1186/S13059-019-1842-9-FIGURES/4>.
60. Mathys, H., Peng, Z., Boix, C.A., Victor, M.B., Leary, N., Babu, S., Abdelhady, G., Jiang, X., Ng, A.P., Ghafari, K., et al. (2023). Single-cell atlas reveals correlates of high cognitive function, dementia, and resilience to

- Alzheimer's disease pathology. *Cell*, 186. <https://doi.org/10.1016/j.cell.2023.08.039>.
61. Silva, E., and Ideker, T. (2019). Transcriptional responses to DNA damage. *DNA Repair* 79, 40–49. <https://doi.org/10.1016/j.dnarep.2019.05.002>.
  62. Cruz, J.C., Tseng, H.C., Goldman, J.A., Shih, H., and Tsai, L.H. (2003). Aberrant Cdk5 activation by p25 triggers pathological events leading to neurodegeneration and neurofibrillary tangles. *Neuron* 40, 471–483. [https://doi.org/10.1016/S0896-6273\(03\)00627-5](https://doi.org/10.1016/S0896-6273(03)00627-5).
  63. Kim, D., Frank, C.L., Dobbin, M.M., Tsunemoto, R.K., Tu, W., Peng, P.L., Guan, J.S., Lee, B.H., Moy, L.Y., Giusti, P., et al. (2008). Deregulation of HDAC1 by p25/Cdk5 in Neurotoxicity. *Neuron* 60, 803–817. <https://doi.org/10.1016/j.neuron.2008.10.015>.
  64. Cruz, J.C., Kim, D., Moy, L.Y., Dobbin, M.M., Sun, X., Bronson, R.T., and Tsai, L.H. (2006). p25/cyclin-dependent kinase 5 induces production and intraneuronal accumulation of amyloid beta in vivo. *J. Neurosci.* 26, 10536–10541. <https://doi.org/10.1523/JNEUROSCI.3133-06.2006>.
  65. Trapnell, C., Cacchiarelli, D., Grimsby, J., Pokharel, P., Li, S., Morse, M., Lennon, N.J., Livak, K.J., Mikkelsen, T.S., and Rinn, J.L. (2014). The dynamics and regulators of cell fate decisions are revealed by pseudotemporal ordering of single cells. *Nat. Biotechnol.* 32, 381–386. <https://doi.org/10.1038/nbt.2859>.
  66. Ramsden, D.A., and Nussenzweig, A. (2021). Mechanisms driving chromosomal translocations: lost in time and space. *Oncogene* 40, 4263–4270. <https://doi.org/10.1038/S41388-021-01856-9>.
  67. Roukos, V., Voss, T.C., Schmidt, C.K., Lee, S., Wangsa, D., and Misteli, T. (2013). Spatial dynamics of chromosome translocations in living cells 341, 660–664.
  68. Canela, A., Maman, Y., Huang, S.Y.N., Wutz, G., Tang, W., Zagnoli-Vieira, G., Callen, E., Wong, N., Day, A., Peters, J.M., et al. (2019). Topoisomerase II-Induced Chromosome Breakage and Translocation Is Determined by Chromosome Architecture and Transcriptional Activity. *Mol. Cell* 75, 252–266.e8. <https://doi.org/10.1016/J.MOLCEL.2019.04.030>.
  69. Yan, W.X., Mirzazadeh, R., Garnerone, S., Scott, D., Schneider, M.W., Kallas, T., Custodio, J., Wernersson, E., Li, Y., Gao, L., et al. (2017). BLISS is a versatile and quantitative method for genome-wide profiling of DNA double-strand breaks. *Nat. Commun.* 8, 15058. <https://doi.org/10.1038/ncomms15058>.
  70. Liu, Y.Y., Tanikawa, C., Ueda, K., and Matsuda, K. (2019). INKA2, a novel p53 target that interacts with the serine/threonine kinase PAK4. *Int. J. Oncol.* 54, 1907–1920. <https://doi.org/10.3892/IJO.2019.4786>.
  71. Lai, C.H., Barik, P., Hsieh, D.J.Y., Day, C.H., Ho, T.J., Chen, R.J., Kuo, W.W., Padma, V.V., Shibu, M.A., and Huang, C.Y. (2020). Inhibition of cell death-inducing p53 target 1 through miR-210-3p overexpression attenuates reactive oxygen species and apoptosis in rat adipose-derived stem cells challenged with Angiotensin II. *Biochem. Biophys. Res. Commun.* 532, 347–354. <https://doi.org/10.1016/J.BBRC.2020.07.052>.
  72. Mijit, M., Caracciolo, V., Melillo, A., Amicarelli, F., and Giordano, A. (2020). Role of p53 in the Regulation of Cellular Senescence. *Biomolecules* 10, 420. <https://doi.org/10.3390/BIOM10030420>.
  73. Wei, P.C., Chang, A.N., Kao, J., Du, Z., Meyers, R.M., Alt, F.W., and Schwer, B. (2016). Long Neural Genes Harbor Recurrent DNA Break Clusters in Neural Stem/Progenitor Cells. *Cell* 164, 644–655. <https://doi.org/10.1016/j.cell.2015.12.039>.
  74. Bellenguez, C., Küçükali, F., Jansen, I.E., Klei, L., Moreno-Grau, S., Amin, N., Naj, A.C., Campos-Martin, R., Grenier-Boley, B., Andrade, V., et al. (2022). New insights into the genetic etiology of Alzheimer's disease and related dementias. *Nat. Genet.* 54, 412–436. <https://doi.org/10.1038/s41588-022-01024-z>.
  75. Sollis, E., Mosaku, A., Abid, A., Buniello, A., Cerezo, M., Gil, L., Groza, T., Güneş, O., Hall, P., Hayhurst, J., et al. (2023). The NHGRI-EBI GWAS Catalog: knowledgebase and deposition resource. *Nucleic Acids Res.* 51, D977–D985. <https://doi.org/10.1093/nar/gkac1010>.
  76. Phillips-Cremins, J.E., Sauria, M.E.G., Sanyal, A., Gerasimova, T.I., Lajoie, B.R., Bell, J.S.K., Ong, C.T., Hookway, T.A., Guo, C., Sun, Y., et al. (2013). Architectural protein subclasses shape 3D organization of genomes during lineage commitment. *Cell* 153, 1281–1295. <https://doi.org/10.1016/j.cell.2013.04.053>.
  77. Rao, S.S.P., Huang, S.C., Glenn St Hilaire, B., Engreitz, J.M., Perez, E.M., Kieffer-Kwon, K.R., Sanborn, A.L., Johnstone, S.E., Bascom, G.D., Bochkov, I.D., et al. (2017). Cohesin Loss Eliminates All Loop Domains. *Cell* 171, 305–320.e24. <https://doi.org/10.1016/j.cell.2017.09.026>.
  78. Caron, P., Aymard, F., Iacovoni, J.S., Briois, S., Canitrot, Y., Bugler, B., Massip, L., Losada, A., and Legube, G. (2012). Cohesin Protects Genes against  $\gamma$ H2AX Induced by DNA Double-Strand Breaks. *PLoS Genet.* 8, e1002460. <https://doi.org/10.1371/JOURNAL.PGEN.1002460>.
  79. Covo, S., Westmoreland, J.W., Gordenin, D.A., and Resnick, M.A. (2010). Cohesin Is limiting for the suppression of DNA damage-induced recombination between homologous chromosomes. *PLoS Genet.* 6, e1001006. <https://doi.org/10.1371/JOURNAL.PGEN.1001006>.
  80. Gelot, C., Guirouilh-Barbat, J., Le Guen, T., Dardillac, E., Chailleux, C., Canitrot, Y., and Lopez, B.S. (2016). The Cohesin Complex Prevents the End Joining of Distant DNA Double-Strand Ends. *Mol. Cell* 61, 15–26. <https://doi.org/10.1016/J.MOLCEL.2015.11.002>.
  81. Hansen, A.S., Cattoglio, C., Darzacq, X., and Tjian, R. (2018). Recent evidence that TADs and chromatin loops are dynamic structures. *Nucleus* 9, 20–32. <https://doi.org/10.1080/19491034.2017.1389365>.
  82. Davidson, I.F., Bauer, B., Goetz, D., Tang, W., Wutz, G., and Peters, J.M. (2019). DNA loop extrusion by human cohesin. *Science* 366, 1338–1345. <https://doi.org/10.1126/science.aaz3418>.
  83. Kim, Y., Shi, Z., Zhang, H., Finkelstein, I.J., and Yu, H. (2019). Human cohesin compacts DNA by loop extrusion. *Science* 366, 1345–1349. <https://doi.org/10.1126/SCIENCE.AAZ4475>.
  84. Nora, E.P., Goloborodko, A., Valton, A.L., Gibcus, J.H., Uebersohn, A., Abdennur, N., Dekker, J., Mirny, L.A., and Bruneau, B.G. (2017). Targeted Degradation of CTCF Decouples Local Insulation of Chromosome Domains from Genomic Compartmentalization. *Cell* 169, 930–944.e22. <https://doi.org/10.1016/j.cell.2017.05.004>.
  85. Solovei, I., Wang, A.S., Thanisch, K., Schmidt, C.S., Krebs, S., Zwerger, M., Cohen, T.V., Devys, D., Foisner, R., Peichl, L., et al. (2013). LBR and lamin A/C sequentially tether peripheral heterochromatin and inversely regulate differentiation. *Cell* 152, 584–598. <https://doi.org/10.1016/j.cell.2013.01.009>.
  86. Etourneau, L., Moussa, A., Rass, E., Genet, D., Willaume, S., Chabance-Okumura, C., Wanschoor, P., Picotto, J., Thézé, B., Dépaigne, J., et al. (2021). Lamin B1 sequesters 53BP1 to control its recruitment to DNA damage. *Sci. Adv.* 7, 3799–3826. <https://doi.org/10.1126/SCIADV.ABB3799>.
  87. Xiong, X., James, B.T., Boix, C.A., Park, Y., Galani, K., Victor, M.B., Sun, N., Hou, L., Dileep, V., Ho, L.-L., et al. (2023). Single-cell epigenomic dissection of Alzheimer's disease pinpoints causal variants and reveals epigenome erosion. *Cell* 186.
  88. Rao, S.S.P., Huntley, M.H., Durand, N.C., Stamenova, E.K., Bochkov, I.D., Robinson, J.T., Sanborn, A.L., Machol, I., Omer, A.D., Lander, E.S., and Aiden, E.L. (2014). A 3D map of the human genome at kilobase resolution reveals principles of chromatin looping. *Cell* 159, 1665–1680. <https://doi.org/10.1016/j.cell.2014.11.021>.
  89. Lieberman-Aiden, E., Van Berkum, N.L., Williams, L., Imakaev, M., Ragoczy, T., Telling, A., Amit, I., Lajoie, B.R., Sabo, P.J., Dorschner, M.O., et al. (2009). Comprehensive mapping of long range interactions reveals folding principles of the human genome. *Science* 326, 289–293. <https://doi.org/10.1126/SCIENCE.1181369>.
  90. van Steensel, B., and Belmont, A.S. (2017). Lamina-Associated Domains: Links with Chromosome Architecture, Heterochromatin, and Gene Repression (NIH Public Access). <https://doi.org/10.1016/j.cell.2017.04.022>.



91. Heinz, S., Benner, C., Spann, N., Bertolino, E., Lin, Y.C., Laslo, P., Cheng, J.X., Murre, C., Singh, H., and Glass, C.K. (2010). Simple combinations of lineage-determining transcription factors prime cis-regulatory elements required for macrophage and B cell identities. *Mol. Cell* 38, 576–589. <https://doi.org/10.1016/J.MOLCEL.2010.05.004>.
92. Yoshiyama, Y., Higuchi, M., Zhang, B., Huang, S.M., Iwata, N., Saido, T.C., Maeda, J., Sahara, T., Trojanowski, J.Q., and Lee, V.M.Y. (2007). Synapse Loss and Microglial Activation Precede Tangles in a P301S Tauopathy Mouse Model. *Neuron* 53, 337–351. <https://doi.org/10.1016/j.neuron.2007.01.010>.
93. Dobbin, M.M., Madabhushi, R., Pan, L., Chen, Y., Kim, D., Gao, J., Ahanonu, B., Pao, P.C., Qiu, Y., Zhao, Y., and Tsai, L.H. (2013). SIRT1 collaborates with ATM and HDAC1 to maintain genomic stability in neurons. *Nat. Neurosci.* 16, 1008–1015.
94. Bonev, B., Mendelson Cohen, N., Szabo, Q., Fritsch, L., Papadopoulos, G.L., Lubling, Y., Xu, X., Lv, X., Hugnot, J.P., Tanay, A., and Cavalli, G. (2017). Multiscale 3D Genome Rewiring during Mouse Neural Development. *Cell* 171, 557–572.e24. <https://doi.org/10.1016/j.cell.2017.09.043>.
95. Hu, B., Won, H., Mah, W., Park, R.B., Kassim, B., Spiess, K., Kozlenkov, A., Crowley, C.A., Pochareddy, S., et al.; PsychENCODE Consortium (2021). Neuronal and glial 3D chromatin architecture informs the cellular etiology of brain disorders. *Nat. Commun.* 12, 3968. <https://doi.org/10.1038/s41467-021-24243-0>.
96. Kim, J.H., Rege, M., Valeri, J., Dunagin, M.C., Metzger, A., Titus, K.R., Gilgenast, T.G., Gong, W., Beagan, J.A., Raj, A., and Phillips-Cremins, J.E. (2019). LADL: light-activated dynamic looping for endogenous gene expression control. *Nat. Methods* 16, 633–639. <https://doi.org/10.1038/s41592-019-0436-5>.
97. Ghavi-Helm, Y., Klein, F.A., Pakozdi, T., Ciglar, L., Noordermeer, D., Huber, W., and Furlong, E.E.M. (2014). Enhancer loops appear stable during development and are associated with paused polymerase. *Nat* 512, 96–100. <https://doi.org/10.1038/nature13417>.
98. Kalocsay, M., Hiller, N.J., and Jentsch, S. (2009). Chromosome-wide Rad51 Spreading and SUMO-H2A.Z-Dependent Chromosome Fixation in Response to a Persistent DNA Double-Strand Break. *Mol. Cell* 33, 335–343. <https://doi.org/10.1016/J.MOLCEL.2009.01.016>.
99. Stefanelli, G., Azam, A.B., Walters, B.J., Brimble, M.A., Gettens, C.P., Bouchard-Cannon, P., Cheng, H.Y.M., Davidoff, A.M., Narkaj, K., Day, J.J., et al. (2018). Learning and Age-Related Changes in Genome-wide H2A.Z Binding in the Mouse Hippocampus. *Cell Rep.* 22, 1124–1131. <https://doi.org/10.1016/J.CELREP.2018.01.020>.
100. Zovkic, I.B., Paulukaitis, B.S., Day, J.J., Etikala, D.M., and Sweatt, J.D. (2014). Histone H2A.Z subunit exchange controls consolidation of recent and remote memory. *Nat* 515, 582–586. <https://doi.org/10.1038/nature13707>.
101. Wang, Z.F., Krasikov, T., Frey, M.R., Wang, J., Matera, A.G., and Marzluft, W.F. (1996). Characterization of the mouse histone gene cluster on chromosome 13: 45 histone genes in three patches spread over 1Mb. *Genome Res.* 6, 688–701. <https://doi.org/10.1101/GR.6.8.688>.
102. Mckinnon, P.J. (2013). Maintaining Genome Stability in the Nervous System. *Nat. Neurosci.* 16, 1523–1529. <https://doi.org/10.1038/NN.3537>.
103. Pollina, E.A., Gilliam, D.T., Landau, A.T., Lin, C., Pajarillo, N., Davis, C.P., Harmin, D.A., Yap, E.L., Vogel, I.R., Griffith, E.C., et al. (2023). A NPAS4–NuA4 complex couples synaptic activity to DNA repair. *Nature* 614, 732–741. <https://doi.org/10.1038/s41586-023-05711-7>.
104. Zhu, Q., Niu, Y., Gundry, M., and Zong, C. (2021). Single-cell damage-nome profiling unveils vulnerable genes and functional pathways in human genome toward DNA damage. *Sci Adv.* 7, eabf3329. <https://doi.org/10.1126/sciadv.abf3329>.
105. Chow, H.M., and Herrup, K. (2015). Genomic integrity and the ageing brain. *Nat. Rev. Neurosci.* 16, 672–684. <https://doi.org/10.1038/nrn4020>.
106. Gao, Y., Sun, Y., Frank, K.M., Dikkes, P., Fujiwara, Y., Seidl, K.J., Sekiguchi, J.M., Rathbun, G.A., Swat, W., Wang, J., et al. (1998). A critical role for DNA end-joining proteins in both lymphogenesis and neurogenesis. *Cell* 95, 891–902. [https://doi.org/10.1016/S0092-8674\(00\)81714-6](https://doi.org/10.1016/S0092-8674(00)81714-6).
107. Shimizu, I., Yoshida, Y., Suda, M., and Minamoto, T. (2014). DNA damage response and metabolic disease. *Cell Metab.* 20, 967–977. <https://doi.org/10.1016/j.cmet.2014.10.008>.
108. Schumacher, B., Pothof, J., Vijg, J., and Hoeijmakers, J.H.J. (2021). The central role of DNA damage in the ageing process. *Nature* 592, 695–703. <https://doi.org/10.1038/s41586-021-03307-7>.
109. Genetic Modifiers of Huntington’s Disease GeM-HD Consortium, Wheeler, V.C., Chao, M.J., Vonsattel, J.P.G., Pinto, R.M., Lucente, D., Abu-Elneel, K., Ramos, E.M., Mysore, J.S., Gillis, T., et al. (2015). Identification of Genetic Factors that Modify Clinical Onset of Huntington’s Disease. *Cell* 162, 516–526. <https://doi.org/10.1016/j.cell.2015.07.003>.
110. Edwards, P.A.W. (2010). Fusion genes and chromosome translocations in the common epithelial cancers. *J. Pathol.* 220, 244–254. <https://doi.org/10.1002/PATH.2632>.
111. Uhrig, S., Ellermann, J., Walther, T., Burkhardt, P., Fröhlich, M., Hutter, B., Toprak, U.H., Neumann, O., Stenzinger, A., Scholl, C., et al. (2021). Accurate and efficient detection of gene fusions from RNA sequencing data. *Genome Res.* 31, 448–460. <https://doi.org/10.1101/GR.257246.119>.
112. Dobin, A., Davis, C.A., Schlesinger, F., Drenkow, J., Zaleski, C., Jha, S., Batut, P., Chaisson, M., and Gingeras, T.R. (2013). STAR: Ultrafast universal RNA-seq aligner. *Bioinformatics* 29, 15–21. <https://doi.org/10.1093/bioinformatics/bts635>.
113. Davidson, N.M., Majewski, I.J., and Oshlack, A. (2015). JAFFA: High sensitivity transcriptome-focused fusion gene detection. *Genome Med.* 7, 43. <https://doi.org/10.1186/s13073-015-0167-x>.
114. Jin, Z., Huang, W., Shen, N., Li, J., Wang, X., Dong, J., Park, P.J., and Xi, R. (2022). Single-cell gene fusion detection by scFusion. *Nat. Commun.* 13, 1084. <https://doi.org/10.1038/s41467-022-28661-6>.
115. Gao, T., Soldatov, R., Sarkar, H., Kurkiewicz, A., Biederstedt, E., Loh, P.R., and Kharchenko, P.V. (2023). Haplotype-aware analysis of somatic copy number variations from single-cell transcriptomes. *Nat. Biotechnol.* 41, 417–426. <https://doi.org/10.1038/s41587-022-01468-y>.
116. Fan, J., Lee, H.O., Lee, S., Ryu, D.E., Lee, S., Xue, C., Kim, S.J., Kim, K., Barkas, N., Park, P.J., et al. (2018). Linking transcriptional and genetic tumor heterogeneity through allele analysis of single-cell RNA-seq data. *Genome Res.* 28, 1217–1227. <https://doi.org/10.1101/gr.228080.117>.
117. Patel, A.P., Tirosh, I., Trombetta, J.J., Shalek, A.K., Gillespie, S.M., Wakimoto, H., Cahill, D.P., Nahed, B.V., Curry, W.T., Martuza, R.L., et al. (2014). Single-cell RNA-seq highlights intratumoral heterogeneity in primary glioblastoma. *Science* 344, 1396–1401. <https://doi.org/10.1126/science.1254257>.
118. Pascarella, G., Hon, C.C., Hashimoto, K., Busch, A., Luginbühl, J., Parr, C., Hin Yip, W., Abe, K., Kratz, A., Bonetti, A., et al. (2022). Recombination of repeat elements generates somatic complexity in human genomes. *Cell* 185, 3025–3040.e6. <https://doi.org/10.1016/J.CELL.2022.06.032>.
119. Jurk, D., Wang, C., Miwa, S., Maddick, M., Korolchuk, V., Tsolou, A., Gonos, E.S., Thrasivoulou, C., Saffrey, M.J., Cameron, K., and von Zglinicki, T. (2012). Postmitotic neurons develop a p21-dependent senescence-like phenotype driven by a DNA damage response. *Aging Cell* 11, 996–1004. <https://doi.org/10.1111/J.1474-9726.2012.00870.X>.
120. Saez-Atienzar, S., and Masliah, E. (2020). Cellular senescence and Alzheimer disease: the egg and the chicken scenario. *Nat. Rev. Neurosci.* 21, 433–444. <https://doi.org/10.1038/s41583-020-0325-z>.
121. Welch, G., and Tsai, L.H. (2022). Mechanisms of DNA damage-mediated neurotoxicity in neurodegenerative disease. *EMBO Rep.* 23, e54217. <https://doi.org/10.15252/EMBR.202154217>.
122. Lodato, M.A., Rodin, R.E., Bohrsen, C.L., Coulter, M.E., Barton, A.R., Kwon, M., Sherman, M.A., Vitzthum, C.M., Luquette, L.J., Yandava, C.N., et al. (2018). Aging and neurodegeneration are associated with increased mutations in single human neurons. *Science* 359, 555–559. <https://doi.org/10.1126/science.aao4426>.

123. Miller, M.B., Huang, A.Y., Kim, J., Zhou, Z., Kirkham, S.L., Maury, E.A., Ziegenfuss, J.S., Reed, H.C., Neil, J.E., Rento, L., et al. (2022). Somatic genomic changes in single Alzheimer's disease neurons. *Nat* 604, 714–722. <https://doi.org/10.1038/s41586-022-04640-1>.
124. Lee, M.H., Siddoway, B., Kaeser, G.E., Segota, I., Rivera, R., Romanow, W.J., Liu, C.S., Park, C., Kennedy, G., Long, T., and Chun, J. (2018). Somatic APP gene recombination in Alzheimer's disease and normal neurons. *Nature* 563, 639–645. <https://doi.org/10.1038/s41586-018-0718-6>.
125. Kousi, M., Boix, C., Park, Y.P., Mathys, H., Sledzieski, S., Peng, Z., Bennett, D.A., Tsai, L.-H., and Kellis, M. (2022). Single-cell mosaicism analysis reveals cell-type-specific somatic mutational burden in Alzheimer's Dementia. Preprint at bioRxiv. <https://doi.org/10.1101/2022.04.21.489103>.
126. McConnell, M.J., Moran, J.V., Abyzov, A., Akbarian, S., Bae, T., Cortes-Ciriano, I., Erwin, J.A., Fasching, L., Flasch, D.A., Freed, D., et al. (2017). Intersection of diverse neuronal genomes and neuropsychiatric disease: The Brain Somatic Mosaicism Network. *Science* 356, eaal1641. <https://doi.org/10.1126/science.aal1641>.
127. Bedrosian, T.A., Quayle, C., Novaresi, N., and Gage, F.H. (2018). Early life experience drives structural variation of neural genomes in mice. *Science* 359, 1395–1399. <https://doi.org/10.1126/science.aah3378>.
128. De Cecco, M., Ito, T., Petrashen, A.P., Elias, A.E., Skvir, N.J., Criscione, S.W., Caligiana, A., Broccoli, G., Adney, E.M., Boeke, J.D., et al. (2019). LINE-1 derepression in senescent cells triggers interferon and inflammation. *Nature* 566, 73–78. <https://doi.org/10.1038/S41586-018-0784-9>.
129. Della Valle, F., Reddy, P., Yamamoto, M., Liu, P., Saera-Vila, A., Bensaddek, D., Zhang, H., Prieto Martinez, J., Abassi, L., Celii, M., et al. (2022). LINE-1 RNA causes heterochromatin erosion and is a target for amelioration of senescent phenotypes in progeroid syndromes. *Sci. Transl. Med.* 14, eabl6057. <https://doi.org/10.1126/scitranslmed.abl6057>.
130. Yang, J.H., Hayano, M., Griffin, P.T., Amorim, J.A., Bonkowski, M.S., Apostolides, J.K., Salfati, E.L., Blanchette, M., Munding, E.M., Bhakta, M., et al. (2023). Loss of epigenetic information as a cause of mammalian aging. *Cell* 186, 305–326.e27. <https://doi.org/10.1016/j.cell.2022.12.027>.
131. Frost, B., Bardai, F.H., and Feany, M.B. (2016). Lamin Dysfunction Mediates Neurodegeneration in Tauopathies. *Curr. Biol.* 26, 129–136. <https://doi.org/10.1016/j.cub.2015.11.039>.
132. Matias, I., Diniz, L.P., Damico, I.V., Araujo, A.P.B., Neves, L.d.S., Vargas, G., Leite, R.E.P., Suemoto, C.K., Nitrini, R., Jacob-Filho, W., et al. (2022). Loss of lamin-B1 and defective nuclear morphology are hallmarks of astrocyte senescence in vitro and in the aging human hippocampus. *Aging Cell* 21, e13521. <https://doi.org/10.1111/ACEL.13521>.
133. Falk, M., Feodorova, Y., Naumova, N., Imakaev, M., Lajoie, B.R., Leonhardt, H., Joffe, B., Dekker, J., Fudenberg, G., Solovei, I., and Mirny, L.A. (2019). Heterochromatin drives compartmentalization of inverted and conventional nuclei. *Nature* 570, 395–399. <https://doi.org/10.1038/s41586-019-1275-3>.
134. Isermann, A., Mann, C., and Rube, C.E. (2020). Histone Variant H2A.J Marks Persistent DNA Damage and Triggers the Secretory Phenotype in Radiation-Induced Senescence. *Int. J. Mol. Sci.* 21, 1–20. <https://doi.org/10.3390/IJMS21239130>.
135. Contrepois, K., Coudereau, C., Benayoun, B.A., Schuler, N., Roux, P.F., Bischof, O., Courbeyrette, R., Carvalho, C., Thuret, J.Y., Ma, Z., et al. (2017). Histone variant H2A.J accumulates in senescent cells and promotes inflammatory gene expression. *Nat. Commun.* 8, 14995–15018. <https://doi.org/10.1038/ncomms14995>.
136. Rube, C.E., Baumert, C., Schuler, N., Isermann, A., Schmal, Z., Glanemann, M., Mann, C., and Scherthan, H. (2021). Human skin aging is associated with increased expression of the histone variant H2A.J in the epidermis. *npj Aging Mech. Dis.* 71, 1–11. <https://doi.org/10.1038/s41514-021-00060-z>.
137. Funk, O.H., Qalieh, Y., Doyle, D.Z., Lam, M.M., and Kwan, K.Y. (2022). Postmitotic accumulation of histone variant H3.3 in new cortical neurons establishes neuronal chromatin, transcriptome, and identity. *Proc. Natl. Acad. Sci. USA* 119, e2116956119. <https://doi.org/10.1073/pnas.2116956119>.
138. Chandra, T., Ewels, P.A., Schoenfelder, S., Furlan-Magaril, M., Wingett, S.W., Kirschner, K., Thuret, J.Y., Andrews, S., Fraser, P., and Reik, W. (2015). Global reorganization of the nuclear landscape in senescent cells. *Cell Rep.* 10, 471–483. <https://doi.org/10.1016/J.CELREP.2014.12.055>.
139. Criscione, S.W., De Cecco, M., Siranosian, B., Zhang, Y., Kreiling, J.A., Sedivy, J.M., and Neretti, N. (2016). Reorganization of chromosome architecture in replicative cellular senescence. *Sci. Adv.* 2, e1500882. <https://doi.org/10.1126/SCIADV.1500882>.
140. Iwasaki, O., Tanizawa, H., Kim, K.D., Kossenkov, A., Nacarelli, T., Tashiro, S., Majumdar, S., Showe, L.C., Zhang, R., and Noma, K.I. (2019). Involvement of condensin in cellular senescence through gene regulation and compartmental reorganization. *Nat. Commun.* 10, 5688–5720. <https://doi.org/10.1038/s41467-019-13604-5>.
141. Zirkel, A., Nikolic, M., Sofiadis, K., Mallm, J.P., Brackley, C.A., Gothe, H., Drechsel, O., Becker, C., Altmüller, J., Josipovic, N., et al. (2018). HMGB2 Loss upon Senescence Entry Disrupts Genomic Organization and Induces CTCF Clustering across Cell Types. *Mol. Cell* 70, 730–744.e6. <https://doi.org/10.1016/j.molcel.2018.03.030>.
142. Lebrigand, K., Magnone, V., Barbry, P., and Waldmann, R. (2020). High throughput error corrected Nanopore single cell transcriptome sequencing. *Nat. Commun.* 11, 4025. <https://doi.org/10.1038/s41467-020-17800-6>.
143. Langmead, B., and Salzberg, S.L. (2012). Fast gapped-read alignment with Bowtie 2. *Nat. Methods* 9, 357–359. <https://doi.org/10.1038/nmeth.1923>.
144. Li, H., and Durbin, R. (2009). Fast and accurate short read alignment with Burrows-Wheeler transform. *Bioinformatics* 25, 1754–1760. <https://doi.org/10.1093/bioinformatics/btp324>.
145. Li, H., Handsaker, B., Wysoker, A., Fennell, T., Ruan, J., Homer, N., Marth, G., Abecasis, G., and Durbin, R.; 1000 Genome Project Data Processing Subgroup (2009). The Sequence Alignment/Map format and SAMtools. *Bioinformatics* 25, 2078–2079. <https://doi.org/10.1093/bioinformatics/btp352>.
146. Anders, S., Pyl, P.T., and Huber, W. (2015). HTSeq—a Python framework to work with high-throughput sequencing data. *Bioinformatics* 31, 166–169. <https://doi.org/10.1093/BIOINFORMATICS/BTU638>.
147. Wolf, F.A., Angerer, P., and Theis, F.J. (2018). SCANPY: Large-scale single-cell gene expression data analysis. *Genome Biol.* 19, 15. <https://doi.org/10.1186/S13059-017-1382-0/FIGURES/1>.
148. Crowell, H.L., Sonesson, C., Germain, P.L., Calini, D., Collin, L., Raposo, C., Malhotra, D., and Robinson, M.D. (2020). muscat detects subpopulation-specific state transitions from multi-sample multi-condition single-cell transcriptomics data. *Nat. Commun.* 11, 6077. <https://doi.org/10.1038/S41467-020-19894-4>.
149. Li, H. (2018). Minimap2: Pairwise alignment for nucleotide sequences. *Bioinformatics* 34, 3094–3100. <https://doi.org/10.1093/bioinformatics/bty191>.
150. Bennett, D.A., Buchman, A.S., Boyle, P.A., Barnes, L.L., Wilson, R.S., and Schneider, J.A. (2018). Religious Orders Study and Rush Memory and Aging Project. *J. Alzheimers Dis.* 64, S161–S189. <https://doi.org/10.3233/JAD-179939>.
151. Bennett, D.A., Wilson, R.S., Schneider, J.A., Evans, D.A., Beckett, L.A., Aggarwal, N.T., Barnes, L.L., Fox, J.H., and Bach, J. (2002). Natural history of mild cognitive impairment in older persons. *Neurology* 59, 198–205. <https://doi.org/10.1212/WNL.59.2.198>.
152. Bennett, D.A., Schneider, J.A., Arvanitakis, Z., Kelly, J.F., Aggarwal, N.T., Shah, R.C., and Wilson, R.S. (2006). Neuropathology of older persons without cognitive impairment from two community-based studies. *Neurology* 66, 1837–1844. <https://doi.org/10.1212/01.WNL.0000219668.47116.E6>.
153. Bennett, D.A., Schneider, J.A., Bienias, J.L., Evans, D.A., and Wilson, R.S. (2005). Mild cognitive impairment is related to Alzheimer disease pathology and cerebral infarctions. *Neurology* 64, 834–841. <https://doi.org/10.1212/01.WNL.0000152982.47274.9E>.
154. Swiech, L., Heidenreich, M., Banerjee, A., Habib, N., Li, Y., Trombetta, J., Sur, M., and Zhang, F. (2015). In vivo interrogation of gene function in the

- mammalian brain using CRISPR-Cas9. *Nat. Biotechnol.* 33, 102–106. <https://doi.org/10.1038/NBT.3055>.
155. Eden, E., Navon, R., Steinfeld, I., Lipson, D., and Yakhini, Z. (2009). GOrilla: A tool for discovery and visualization of enriched GO terms in ranked gene lists. *BMC Bioinf.* 10, 48. <https://doi.org/10.1186/1471-2105-10-48/TABLES/1>.
156. Bates, D., Mächler, M., Bolker, B., and Walker, S. (2015). Fitting linear mixed-effects models using lme4. *J. Stat. Softw.* 67. <https://doi.org/10.18637/jss.v067.i01>.

## STAR★METHODS

### KEY RESOURCES TABLE

REAGENT or RESOURCE	SOURCE	IDENTIFIER
<b>Antibodies</b>		
Anti-Lamin B1	Abcam	Cat#ab16048; RRID:AB_443298
Anti-H2A.X-Phosphorylated (Ser139) Antibody, APC conjugated	BioLegend	Cat#613416; RRID:AB_2629534
Anti-NeuN, clone A60, Alexa Fluor 488 conjugated	EMD Millipore	Cat#MAB377X; RRID:AB_2149209
Anti-RAD21	Millipore Sigma	Cat#05-908; RRID:AB_417383
Anti-NeuN	Synaptic Systems	Cat#266 004; RRID:AB_2619988
Anti-H2A.X-Phosphorylated (Ser139)	Millipore	Cat#05-636; RRID:AB_309864
Alexa Fluor 488 (Donkey anti-Rabbit)	Thermo Fisher Scientific	Cat#A-21206; RRID:AB_2535792
Alexa Fluor 594 (Goat anti-Guinea Pig)	Thermo Fisher Scientific	Cat#A-11076; RRID:AB_141930
Alexa Fluor 647 (Donkey anti-Mouse)	Thermo Fisher Scientific	Cat#A-31571; RRID:AB_162542
Alexa Fluor 488 (Goat anti-Guinea Pig)	Thermo Fisher Scientific	Cat#A-11073; RRID:AB_2534117
Alexa Fluor 594 (Goat Anti-Mouse)	Thermo Fisher Scientific	Cat#A-11032; RRID:AB_2534091
<b>Biological samples</b>		
Human brain tissue	Religious Orders Study or Rush Memory and Aging Project	<a href="#">Table S1</a> , page 1
Human brain tissue	Massachusetts Alzheimer's Disease Research Center	<a href="#">Table S1</a> , page 5
<b>Chemicals, peptides, and recombinant proteins</b>		
Dynabeads™ M-280 Streptavidin	Thermo Fisher Scientific	Cat#11205D
Dynabeads® MyOne™ Streptavidin C1	Thermo Fisher Scientific	Cat#65001
GlycoBlue™ Coprecipitant (15 mg/mL)	Ambion by Life Technologies	Cat#AM9515
RiboSafe RNase Inhibitor, 2500 Units	Bioline	Cat#BIO-65027
Bovine Serum Albumin (IgG-Free, Protease-Free)	Jackson ImmunoResearch Laboratories, Inc.	Cat#001-000-162
Quick Ligase Kit	New England Biolabs (NEB)	Cat#M2200S
Proteinase K	New England Biolabs	Cat#P8107S
Q5® High-Fidelity Master Mix, 2X	New England Biolabs (NEB)	Cat#M0492S
NEBNext Multiplex Oligos for Illumina (96 Unique Dual Index)	New England Biolabs (NEB)	Cat#E6440S
T4 Polynucleotide Kinase	New England Biolabs (NEB)	Cat#M0201S
Klenow Fragment (3'-5' exo-)	New England Biolabs (NEB)	Cat#M0212S
Mbol (25,000 units/ml)	New England Biolabs (NEB)	Cat#R0147M
T4 DNA Ligase (2,000,000 units/ml)	New England Biolabs (NEB)	Cat#M0202M
BSA, Molecular Biology Grade	New England Biolabs (NEB)	Cat#B9000S
CutSmart Buffer - 5.0 mL	New England Biolabs (NEB)	Cat#B7204S
Adenosine-5 Triphosphate (ATP) - 1 mL	New England Biolabs (NEB)	Cat#P0756S
T4 RNA Ligase 2, truncated KQ - 10,000 units	New England Biolabs (NEB)	Cat#M0373L
Dnase I (RNase-Free)	New England Biolabs (NEB)	Cat#M0303S
T4 DNA Ligase Reaction Buffer	New England Biolabs (NEB)	Cat#B0202S
T4 DNA Polymerase	New England Biolabs (NEB)	Cat#M0203S
DNA Polymerase I, Large (Klenow) Fragment	New England Biolabs (NEB)	Cat#M0210S

(Continued on next page)



**Continued**

REAGENT or RESOURCE	SOURCE	IDENTIFIER
Deoxynucleotide Solution Mix - 8 μmol of each	New England Biolabs (NEB)	Cat#N0447S
T4 DNA Ligase	New England Biolabs (NEB)	Cat#M0202S
Pierce™ 16% Formaldehyde (w/v), Methanol-free	Thermo Fisher Scientific	Cat#28908
dNTP mix (25mM)	Thermo Fisher Scientific	Cat#R1121
RNase A, DNase and protease-free (10 mg/mL)	Thermo Fisher Scientific	Cat#EN0531
Biotin-14-dATP	Thermo Fisher Scientific	Cat#19524016
DAPI	Millipore Sigma	Cat#D9542-1MG
Recombinant RNase Inhibitor	Takara	Cat#2313A
OptiPrep™	StemCell Technologies	Cat#7820
NucBlue™ Live ReadyProbes™	Thermo Fisher Scientific	Cat#R37605
Buffer TCL	QIAGEN	Cat#1031576
Agencourt RNAClean XP	Beckman Coulter	Cat#A63987
KAPA HiFi HotStart ReadyMix	Roche	Cat#KK2602
Maxima H Minus Reverse Transcriptase	Thermo Fisher Scientific	Cat#EP0753
Agencourt AMPure XP bead	Beckman Coulter	Cat#A63881
Fluoromount-G™ Slide Mounting Medium	VWR	Cat#100502-406
HBSS	Thermo Fisher Scientific	Cat#14175103
Papain	Worthington Biochemical Corp	Cat#LS003126
DNase I	Roche	Cat#10104159001
Neurobasal media	Thermo Fisher Scientific	Cat#21103049
1% Penicillin/Streptomycin Solution	Gemini Bio-Products	Cat#400-109
B-27	Invitrogen	Cat#17504-044
GlutaMAX Supplement	Thermo Fisher Scientific	Cat#35050-079
Recombinant RNase Inhibitor	Takara	Cat#2313A
NucBlue Live ReadyProbes Reagent	Thermo Fisher Scientific	Cat#R37605
Buffer TCL	QIAGEN	Cat#1031576
Beta-mercaptoethanol	Sigma-Aldrich	Cat#M6250
Agencourt RNAClean XP beads	Beckman Coulter	Cat#A63987
Maxima H Minus Reverse Transcriptase	Thermo Fisher	Cat#EP0753
KAPA HiFi HotStart ReadyMix	KAPA Biosystems	Cat#KK2602
Agencourt AMPure XP bead	Beckman Coulter	Cat#A63881
Nextera XT DNA Library Preparation Kit	Illumina	Cat#FC-131-1096
Q5® High-Fidelity 2X Master Mix	New England Biolabs	Cat#M0492S
Ligation Sequencing Kit	Oxford Nanopore Technology	Cat#SQK-LSK109
Native Barcoding Kit 24 V14	Oxford Nanopore Technology	Cat#SQK-NBD114.24
Protease inhibitors	Roche	Cat#11836170001
RNase inhibitors	Thermo Fisher Scientific	Cat#EO0382
Lysis buffer	Sigma	Cat#NUC201-1KT

**Critical commercial assays**

Dovetail™ Hi-C Kit	Dovetail Genomics	Cat#21004
Nextera Mate Pair Library Prep Kit (12 indexes, 48 gel-free samples or 12 gel-plus samples)	Illumina	Cat#FC-132-1001
Qubit dsDNA HS Assay Kit	Invitrogen	Cat#Q32851
NEBNext Ultra II DNA Library Prep Kit for Illumina	New England Biolabs (NEB)	Cat#E7645S

(Continued on next page)

**Continued**

REAGENT or RESOURCE	SOURCE	IDENTIFIER
HiScribe T7 High Yield RNA Synthesis Kit	New England Biolabs (NEB)	Cat#E2040S
NEBNext End Repair Module	New England Biolabs (NEB)	Cat#E6050S
NEBNext dA-Tailing Module	New England Biolabs (NEB)	Cat#E6053S
SuperScript™ IV First-Strand Synthesis System	Thermo Fisher Scientific	Cat#18091050
DNA Clean & Concentrator-5 with Zymo-Spin IC Columns, Capped, 50 Preps	Zymo Research	Cat#D4013
Nextera XT DNA Library Preparation Kit	Illumina	Cat#FC-131-1096
Ligation Sequencing Kit	Oxford Nanopore Technology	Cat#SQK-LSK109
Native Barcoding Kit 24 V14	Oxford Nanopore Technology	Cat#SQK-NBD114.24

**Deposited data**

Hi-C	This paper	GEO: GSE227445
BLISS	This paper	GEO: GSE227445
Mate-Pair sequencing	This paper	GEO: GSE227445
Human SMART-seq single-nucleus RNA-seq	This paper	SYNAPSE : <a href="https://www.synapse.org/#!Synapse:syn52293417">https://www.synapse.org/#!Synapse:syn52293417</a>
Human 10X single-nucleus RNA_seq	Mathys et al. 2023 <sup>60</sup>	SYNAPSE : <a href="https://www.synapse.org/#!Synapse:syn52293417">https://www.synapse.org/#!Synapse:syn52293417</a>
CK-p25 SMART-seq single-nucleus RNA-seq	Welch et al. 2022 <sup>58</sup>	GEO: GSE174265
Bulk RNA-seq	Welch et al. 2022 <sup>58</sup>	GEO: GSE174265

**Experimental models: Organisms/strains**

CFW® Mice (Swiss Webster) E15 embryos	Charles River	Strain Code: 024
C57BL/6-Tg(tetO-CDK5R1/GFP)337Lht/J	Jackson Laboratory	Stock No: 005706
B6; CBA-Tg(Camk2a-tTA)1Mmay/J	Jackson Laboratory	Stock No: 003010
Tau P301S-tg; B6; C3-Tg(Prnp-MAPT*P301S)PS19Vle/J	Jackson Laboratory	Stock No: 008169

**Oligonucleotides**

NNNCTACACGACGCTCTTC CGATCT (ONT primer)	Lebrigand et al. 2020 <sup>142</sup>	N/A
NNNAAGCAGTGGTATCAACGCA GAGTACAT (ONT primer)	Lebrigand et al. 2020 <sup>142</sup>	N/A
BLISS adaptors and primers	Yan et al. 2017 <sup>69</sup>	Table S1, page 17

**Software and algorithms**

Imarisx64 9.2.1	Bitplane	<a href="http://www.bitplane.com/Default.aspx">http://www.bitplane.com/Default.aspx</a>
Bowtie2	Langmead and Salzberg, 2012 <sup>143</sup>	<a href="http://bowtie-bio.sourceforge.net/bowtie2/index.shtml">http://bowtie-bio.sourceforge.net/bowtie2/index.shtml</a>
Burrows-Wheeler Aligner (BWA)	Li and Durbin, 2009 <sup>144</sup>	<a href="http://bio-bwa.sourceforge.net/">http://bio-bwa.sourceforge.net/</a>
Juicer	Rao et al., 2014 <sup>77</sup>	<a href="https://github.com/aidenlab/juicer/wiki">https://github.com/aidenlab/juicer/wiki</a>
Homer	Heinz et al. 2010 <sup>91</sup>	<a href="http://homer.ucsd.edu/homer/interactions2/index.html">http://homer.ucsd.edu/homer/interactions2/index.html</a>
BEDTools	N/A	<a href="https://bedtools.readthedocs.io/en/latest/">https://bedtools.readthedocs.io/en/latest/</a>
Samtools	Li et al., 2009 <sup>145</sup>	<a href="http://samtools.sourceforge.net/">http://samtools.sourceforge.net/</a>
R	N/A	<a href="https://www.r-project.org/">https://www.r-project.org/</a>
STAR (v.2.7.3)	Dobin et al., 2013 <sup>112</sup>	<a href="https://github.com/alexdobin/STAR/releases?page=2">https://github.com/alexdobin/STAR/releases?page=2</a>
HTSeq-count	Anders et al. 2015 <sup>146</sup>	<a href="https://htseq.readthedocs.io/en/master/">https://htseq.readthedocs.io/en/master/</a>
SCANPY	Wolf et al. 2018 <sup>147</sup>	<a href="https://scanpy.readthedocs.io/en/stable/">https://scanpy.readthedocs.io/en/stable/</a>
Muscat	Crowell et al. 2020 <sup>148</sup>	<a href="https://bioconductor.org/packages/release/bioc/html/muscat.html">https://bioconductor.org/packages/release/bioc/html/muscat.html</a>

(Continued on next page)

**Continued**

REAGENT or RESOURCE	SOURCE	IDENTIFIER
STAR-Fusion v1.10.1	Haas et al. 2019 <sup>59</sup>	<a href="https://github.com/STAR-Fusion/STAR-Fusion/">https://github.com/STAR-Fusion/STAR-Fusion/</a>
minimap2 (v2.22-r1101)	Li. 2018 <sup>149</sup>	<a href="https://github.com/lh3/minimap2">https://github.com/lh3/minimap2</a>
cutadapt	N/A	<a href="https://cutadapt.readthedocs.io/en/stable/">https://cutadapt.readthedocs.io/en/stable/</a>
Monocle3	Trapnell et al. 2014 <sup>65</sup>	<a href="https://cole-trapnell-lab.github.io/monocle3/">https://cole-trapnell-lab.github.io/monocle3/</a>
<b>Other</b>		
microTUBE AFA Fiber Pre-Slit Snap-Cap 6x16mm	Covaris	Cat#520045
MatTek 35 mm Dish, No. 1.0 Coverslip, 14 mm Glass Diameter, Poly-D-Lysine Coated	MatTek Corporation	Cat#P35GC-1.0-14-C
Mini Cell Scrapers	ABI Scientific Inc.	Cat#MCS-200
Fisherbrand™ Superfrost™ Plus Microscope Slides	Thermo Fisher Scientific	Cat#12-550-15
100 μM cell strainer	VWR	Cat#21008-950
Countess II Automated Cell Counter	Thermo Fisher Scientific	Cat#AMQAX1000
40 μm cell strainer	Falcon Cell Strainers, Sterile, Corning	Cat#352340
70 μm cell strainer	VWR	Cat#21008-952
Ultra-Clear Centrifuge Tubes, 1 × 3.5 in. (25 × 89 mm)	Beckman	Cat#344058
Poly-D-Lysine-coated coverslips	VWR	Cat#194310012A

**RESOURCE AVAILABILITY**

**Lead contact**

Further information and requests for resources and reagents should be directed to and will be fulfilled by the lead contact, Li-Huei Tsai ([lhtsai@mit.edu](mailto:lhtsai@mit.edu)).

**Materials availability**

This study did not generate new unique reagents.

**Data and code availability**

- Single-nucleus RNA-seq data will be available through the AD Knowledge Portal on Synapse upon publication of this manuscript. The data are available here: <https://www.synapse.org/#!Synapse:syn52293417>. The data are available under controlled use conditions set by human privacy regulations. To access the data, a data use agreement is needed. This registration is in place solely to ensure the anonymity of the ROSMAP study participants. A data use agreement can be agreed with either Rush University Medical Center (RUMC) or with SAGE, which maintains Synapse, and can be downloaded from their websites (<https://adknowledgeportal.synapse.org/>).
- All mouse data generated in this study, including raw and processed files, are available at GEO: GSE227445.
- We have established a web portal for this paper at [http://compbio.mit.edu/ad\\_dna\\_damage/](http://compbio.mit.edu/ad_dna_damage/) to better describe and provide access to our datasets and code, which is also available on Zenodo (8290268, <https://doi.org/10.5281/zenodo.8290268>).
- Any additional information required to reanalyze the data reported in this paper is available from the **lead contact** upon request

**EXPERIMENTAL MODEL AND STUDY PARTICIPANT DETAILS**

**Human subjects**

We selected 427 individuals from the Religious Orders Study and Rush Memory and Aging Project (ROSMAP), both ongoing longitudinal clinical-pathologic cohort studies of aging and dementia, in which all participants are brain donors. The studies include clinical data collected annually, detailed postmortem pathological evaluations, and extensive genetic, epigenomic, transcriptomic, proteomic, and metabolomic bulk-tissue profiling.<sup>150</sup> Individuals were balanced between sexes (male:female ratio 212:215). Informed consent was obtained from each subject, and the Religious Orders Study and Rush Memory and Aging Project were each approved by an Institutional Review Board (IRB) of Rush University Medical Center. Participants also signed an Anatomic Gift Act, and a

repository consent to allow their data to be repurposed. Participants enrolled without known dementia and agreed to annual clinical evaluation and organ donation.

For single-nucleus Smart-seq2, we selected a subset of 47 individuals comprised of 24 and 23 age and sex-matched cases with AD pathology (NIA-Reagan 1–2) and no pathologic AD (NIA-Reagan 3–4). For the gene fusion burden analysis, we additionally split the samples independent of NIA-Reagan by.

- 1) Braak stage (Bennett et al., 2005), where stages 1–4 indicate the absence of NFTs in the prefrontal cortex (PFC) and stages 5–6 indicate the presence of NFTs in the PFC.
- 2) Clinical diagnosis (variable cogdx), where 1–3 indicate no or mild cognitive impairment and 4–5 indicate AD dementia.<sup>151,152</sup>

### Animal models

All the experiments were approved by the Committee for Animal Care of the Division of Comparative Medicine at the Massachusetts Institute of Technology (MIT) and carried out at MIT. Tg(Camk2a-tTA) and Tg(Prnp-MAPT\*P301S)PS19 were obtained from the Jackson laboratory. Tg(tetO-CDK5R1/GFP) was generated in our lab. All the transgenic mice were bred and maintained in our animal facility. We used male TauP301S mice at 3 months and 11–12 months of age. CK-p25 mice are generated by breeding CaMKII $\alpha$  promoter-tTA mice (CK controls) with tetO-CDK5R1/GFP mice and raised on doxycycline-containing food to repress p25 expression. CKp-p25 mice were induced for 1, 2, or 6 weeks depending on the experiment by replacing the doxycycline diet with a normal rodent diet. We used adult CK-p25 mice (4–8 months old) for all experiments. Both male and female mice were used for Hi-C, and female mice were used for all other experiments.

### Primary neuron culture

Cortices were dissected from E15 Swiss-Webster embryos in ice-cold HBSS (Thermo Fisher Scientific, 14175103) and dissociated with papain (Worthington Biochemical Corp, LS003126) and DNase I (Roche, 10104159001). Cells were resuspended in plating media (Neurobasal media (Thermo Fisher Scientific, 21103049), 1% Penicillin/Streptomycin Solution (Gemini Bio-Products, 400-109), 10% FBS) and filtered through a 100  $\mu$ M cell strainer (VWR, 21008-950). Cell density was quantified using a Countess II Automated Cell Counter (Thermo Fisher Scientific, AMQAX1000), then plated on poly-D-Lysine-coated 12-well culture dishes at  $0.5 \times 10^6$  cells or in 100 mm culture dishes at  $5 \times 10^6$  cells. Cultures were maintained in 5% CO<sub>2</sub> at 37 °C in a cell culture incubator. After allowing four hours for the cells to adhere to the plate, the media was replaced and maintained with neurobasal media supplemented with B-27 (Invitrogen, 17504-044), 1% Penicillin/Streptomycin, and 1% GlutaMAX Supplement (Thermo Fisher Scientific, 35050-079).

### MADRC brain tissue samples

Immunohistochemistry was performed using fresh frozen postmortem PFC brain samples which were generously provided by the Massachusetts Alzheimer's Disease Research Center (MADRC). Sample selection was based on the Braak staging. Braak stage,<sup>153</sup> where stages 1–4 indicate the absence of NFTs in the prefrontal cortex (PFC), and stages 5–6 indicate the presence of NFTs in the PFC. The three samples identified as AD had a Braak score of 5 or above. Meanwhile, the remaining three non-AD samples had Braak scores less than or equal to 3. For more information on the samples, the sample metadata can be found in Supplementary Table S1, page 15.

## METHOD DETAILS

### Single-nucleus Smart-seq2

We adapted the protocol for the isolation of nuclei from frozen postmortem brain tissue from Swiech et al. 2015.<sup>154</sup> All procedures were carried out on ice or at 4°C. Briefly, postmortem brain tissue was homogenized in 2 mL Homogenization Buffer (320 mM Sucrose, 5 mM CaCl<sub>2</sub>, 3 mM Mg(Ac)<sub>2</sub>, 10 mM Tris-HCl pH 7.8, 0.1 mM EDTA pH 8.0, 0.1% IGEPAL CA-630, 1 mM  $\beta$ -mercaptoethanol, 0.4 U/microliter Recombinant RNase Inhibitor (Takara, 2313A) using a Wheaton Dounce Tissue Grinder (10 strokes with the loose pestle). 3 mL of Homogenization Buffer was added (final volume 5 mL) and the homogenized tissue was incubated on ice for 5 min. Then the homogenized tissue was filtered through a 40  $\mu$ m cell strainer, mixed with an equal volume of Working Solution (83% OptiPrep Density Gradient Medium (Sigma-Aldrich), 5 mM CaCl<sub>2</sub>, 3 mM Mg(Ac)<sub>2</sub>, 10 mM Tris HCl pH 7.8, 0.1 mM EDTA pH 8.0, 1 mM  $\beta$ -mercaptoethanol) and loaded on top of an OptiPrep density gradient (10 mL 29% OptiPrep solution (29% OptiPrep Density Gradient Medium, 134 mM Sucrose, 5 mM CaCl<sub>2</sub>, 3 mM Mg(Ac)<sub>2</sub>, 10 mM Tris-HCl pH 7.8, 0.1 mM EDTA pH 8.0, 1 mM  $\beta$ -mercaptoethanol, 0.04% IGEPAL CA-630, 0.17 U/microliter Recombinant RNase Inhibitor) on top of 5 mL 35% OptiPrep solution (35% OptiPrep Density Gradient Medium, 96 mM Sucrose, 5 mM CaCl<sub>2</sub>, 3 mM Mg(Ac)<sub>2</sub>, 10 mM Tris-HCl pH 7.8, 0.1 mM EDTA pH 8.0, 1 mM  $\beta$ -mercaptoethanol, 0.03% IGEPAL CA-630, 0.12 U/microliter Recombinant RNase Inhibitor)). The nuclei were separated by ultracentrifugation using an SW32 rotor (20 min, 9000 rpm, 4°C). 3 mL of nuclei were collected from the 29%/35% interphase and washed with 15 mL ice-cold PBS containing 0.5% BSA and 2 mM EDTA. The nuclei were centrifuged at 100 g for 5 min (4 °C) and resuspended in 1 mL PBS containing 0.5% BSA and 2 mM EDTA. Then the nuclei were stained by adding two drops of NucBlue Live ReadyProbes Reagent (ThermoFisher Scientific, R37605) and passed through a 40  $\mu$ m cell strainer (Falcon Cell



Strainers, Sterile, Corning, 352340). Single Hoechst-positive nuclei were sorted into 96-well plates (Eppendorf twin.tec PCR Plate 96, 951020401) containing 5  $\mu$ L of Buffer TCL (QIAGEN, 1031576) per well containing 1% beta-mercaptoethanol (Sigma-Aldrich, M6250), snap frozen on dry ice, and then stored at  $-80^{\circ}\text{C}$  before whole transcriptome amplification, library preparation, and sequencing.

Single-nucleus RNA sequencing libraries were generated based on the Smart-Seq2 protocol<sup>57</sup> with the following modifications. RNA from single cells was first purified with Agencourt RNAClean XP beads (Beckman Coulter, A63987) before oligo-dT primed reverse transcription with Maxima H Minus Reverse Transcriptase (Thermo Fisher, EP0753), which was followed by 21 cycle PCR amplification using KAPA HiFi HotStart ReadyMix (KAPA Biosystems, KK2602) with subsequent Agencourt AMPure XP bead (Beckman Coulter, A63881) purification. Libraries were tagmented using the Nextera XT DNA Library Preparation Kit (Illumina, FC-131-1096) and the Nextera XT Index Kit v2 Sets A, B, C, and D according to the manufacturer's instructions with minor modifications. Specifically, reactions were run at one-fourth the recommended volume, the tagmentation step was extended to 10 min, and the extension time during the PCR step was increased from 30 s to 60 s. Libraries from 192 cells with unique barcodes were combined and sequenced on the Illumina HiSeq 2000 platform at the MIT BioMicro Center.

### Oxford nanopore Technology (ONT) sequencing and analysis

We selected two AD subjects (Female, age = 83, NIA-Regan = 2 and Male, age = 76, NIA-Regan = 1) from the Mathys et al.<sup>60</sup> cohort to perform Oxford Nanopore Long-read sequencing. cDNA (2–10 ng) from the 10x snRNA-seq pipeline was amplified using custom universal primers NNNCTACACGACGCTCTCCGATCT and NNNAAGCAGTGGTATCAACGCAGAGTACAT using Q5 High-Fidelity 2X Master Mix (New England Biolabs, M0492S) for 10 cycles. Amplified cDNA libraries were purified with 0.65x SPRISelect and ONT sequencing libraries were prepared with the Ligation Sequencing Kit (ONT, SQK-LSK109) (PCR-free) and barcode using Native Barcoding Kit 24 V14 (ONT, SQK-NBD114.24) according to the manufacturer's instructions.<sup>142</sup>

### Fluorescence-activated nuclei sorting

Frozen forebrains were disrupted with a loose Dounce homogenizer (30 strokes) in ice-cold PBS with protease inhibitors (Roche, 11836170001) and RNase inhibitors (Thermo Fisher Scientific, EO0382). Samples were fixed with 1% formaldehyde for 10 min at room temperature, then quenched with 2.5 M glycine for 5 min. Homogenized tissue was centrifuged at 1000 g at  $4^{\circ}\text{C}$  for 5 min and the pellet was suspended in lysis buffer (Sigma, Nuclei PURE Prep, NUC201-1KT) followed by dounce-homogenization using the tight pestle (30 strokes) followed by filtration with a 70  $\mu$ M cell strainer (VWR, 21008-952). Nuclei were isolated through sucrose gradient centrifugation (Ultra-Clear Centrifuge Tubes, 1  $\times$  3.5 in. (25  $\times$  89 mm), Beckman, 344058) at 30,000xg for 45 min at  $4^{\circ}\text{C}$  as per manufacturer's instructions for Sigma Nuclei PURE Prep. Primary neuronal cultures were processed as described above, except the cells were fixed in the dish and scraped using a cell scraper. The following antibodies were used to immunostain nuclei: anti-H2A.X-Phosphorylated (Ser139) antibody conjugated to APC (BioLegend, 613416), anti-NeuN antibody conjugated to Alexa Fluor 488 (EMD Millipore, MAB377X). Antibodies were incubated with nuclei in 1% BSA/PBS at  $4^{\circ}\text{C}$  for one hour or overnight. Samples were strained through a 40 $\mu$ m filter (VWR, 21008-949) and stained with DAPI (Sigma Aldrich, D9542) before sorting. Sorting was performed on a FACS Aria at the Koch Institute Flow Cytometry Core (BD Biosciences, US).

### In situ Hi-C

*In situ* Hi-C was performed as previously described in Rao et al., 2014.<sup>88</sup> 80–120k FANS isolated nuclei were used for CK-p25. Nuclei were permeabilized. DNA was digested with 100 units of Mbol, and the ends of restriction fragments were labeled using biotinylated nucleotides and ligated in a small volume. After reversal of crosslinks, ligated DNA was purified and sheared to a length of  $\sim$ 400 bp, at which point ligation junctions were pulled down with streptavidin beads and prepped for Illumina sequencing. Illumina libraries were sequenced in 38 bp paired-end mode. Three replicates were performed, where each replicate was a pool of 3 CK-p25 mice forebrains (Table S1, page 16). P301S Tau mice and primary neuronal culture Hi-C were performed using 120–170k FANS isolated nuclei with the Dovetail Hi-C kit (SKU: 21004) according to the manufacturer's instructions.

### Break-Labeling *in situ* and sequencing (BLISS)

BLISS was performed as previously described with minor modifications.<sup>69</sup> Sorted neurons were attached to a MatTek 35 mm dish, No. 1.0 Coverslip, 14 mm Glass Diameter, Poly-D-Lysine Coated (P35GC-1.0-14-C) by adding the cells to the center coverslip in 4% formaldehyde in PBS and spinning at 2000xg for 2 min. The attached nuclei were then end-repaired using the NEBNext End Repair Module (New England Biolabs, E6050S) and A-tailed using the NEBNext dA-Tailing Module (New England Biolabs, E6053S), with washes using cold PBS and equilibrations using 1X CutSmart Buffer (New England Biolabs, B7204S) performed between the reactions. BLISS adaptors with unique barcodes were ligated to respective samples overnight at  $16^{\circ}\text{C}$  using the T4 DNA Ligase (2,000,000 units/ml) (New England Biolabs, M0202M). The excess BLISS adaptors were removed using a High Salt Buffer wash according to the original protocol. Nuclei were then scraped off the coverslip using a mini scraper and DNA extraction buffer with proteinase K. Samples were reverse cross-linked overnight at  $55^{\circ}\text{C}$ , and genomic DNA was isolated using ethanol precipitation, adding 1  $\mu$ L GlycoBlue Coprecipitant (Ambion by Life Technologies, AM9515), 0.1 volume 3M NaoAc, and 2.5 volumes of 100% ethanol, followed by overnight incubation at  $-80^{\circ}\text{C}$  and ethanol wash. The purified DNA was sonicated to an average size of 500 bp and was then *in-vitro* transcribed using the HiScribe T7 High Yield RNA Synthesis Kit (New England Biolabs, E2040S) for 14 h. Following this,

template DNA was removed by incubating the *in-vitro* transcription (IVT) products with 1  $\mu$ L of DNaseI (RNase-Free) (New England Biolabs, M0303S) for 15 min, and the RNA was purified using RNAXP clean beads. The RA3 adapter (5rApp/TGG AAT TCT CGG GTG CCA AGG/3SpC3/) was ligated onto the RNA using T4 RNA Ligase 2, truncated (New England Biolabs, M0242L). The RNA was then reverse transcribed using the reverse primers RTP (5'-GCCTTGGCACCCGAGAATTCCA-3') and the SuperScript IV First-Strand Synthesis System (Thermo Fisher Scientific, 18091050). Lastly, the DNA was amplified using the Q5 High-Fidelity Master Mix, 2X (New England Biolabs, M0492S) using RP1 and RPI primers for 16–17 cycles. The libraries were purified using 0.8X volume AMPure beads and sequenced using single-end 75 bp reads on an Illumina NextSeq 500.

### Mate-pair sequencing

Mate-pair sequencing was performed using Nextera Mate Pair Library Prep Kit (Illumina, FC-132-1001). Briefly, formaldehyde-fixed FANS sorted nuclei were reverse crosslinked, and genomic DNA was purified. Genomic DNA was tagmented to a size range of 1–5 kb using mate pair transposome containing biotinylated adaptors followed by strand displacement to repair single-stranded gaps. Tagmented genomic DNA was circularized and then fragmented using sonication. The junctions were purified using streptavidin beads. Sequencing libraries were prepared using TruSeq DNA LT Sample Prep (Illumina, 15027084) provided with the mate pair kit or NEBNext Ultra II DNA Library Prep Kit for Illumina (NEB, E7645S) and NEBNext Multiplex Oligos for Illumina (NEB, E6440S). Illumina libraries were sequenced in 75bp or 40bp paired-end mode using Nextseq500.

Minor modifications were made to the manufacturer's instructions to account for the lower amount of genomic DNA from FANS isolated nuclei used for the assay as described below. A minimum of 100k nuclei obtained by FANS was used for the experiments. Samples were reverse-crosslinked in a 300  $\mu$ L reaction with 0.2 M NaCl, 0.5% SDS, and 4 U of Proteinase K (NEB, P8107S) and heating at 95°C for 30 min with shaking at 900 rpm. An additional 4 U of Proteinase K was added and incubated at 55°C for 30 min. DNA was purified by ethanol precipitation by adding 1  $\mu$ L GlycoBlue Coprecipitant (Ambion by Life Technologies, AM9515), 0.1 volume 3 M NaOAc, and 2.5 volumes of 100% ethanol, followed by overnight incubation at –80°C and ethanol wash. Genomic DNA was re-suspended in Tris-EDTA buffer and quantified using Qubit dsDNA HS Assay Kit (Invitrogen, Q32851). A maximum of 250 ng of DNA was used to proceed with mate-pair sequencing protocol as described per the manufacturer's instructions. All reactions were performed at 0.5X volume unless otherwise noted. Tagmentation was performed using 0.25X Tn5 enzyme for 30 min. Circulation was performed in 124  $\mu$ L instead of 300  $\mu$ L and all reagents were scaled down accordingly. Circularized DNA was sheared using Covaris E220 using microTUBE AFA Fiber Pre-Slit Snap-Cap 6  $\times$  16mm (Covaris, 520045) to an average size of 500 bp. Purification of biotinylated DNA was performed using 0.5x the recommended amount of Dynabeads M-280 Streptavidin (Thermo Fisher Scientific, 11205D). The final PCR amplification was done in 50  $\mu$ L according to the kit instructions. Illumina libraries were sequenced in 75 bp paired-end mode.

### Immunofluorescence microscopy

Mice were transcidentally perfused with ice-cold PBS, then fixed with ice-cold 4% paraformaldehyde in PBS. Dissected mouse brains or human brain tissue were drop-fixed overnight in 4% paraformaldehyde in PBS at 4°C. Brain tissue or entire forebrains (mice) were sectioned with a vibrating microtome (Leica BioSystems, Wetzlar Germany) to generate 40  $\mu$ M coronal slices. Slices were blocked for two hours at room temperature in blocking buffer (10% NGS, 0.3% Triton X-100, PBS), then incubated with primary antibody overnight at 4°C. Slices were washed 3  $\times$  10 min with PBS, and Alexa Fluor Secondary antibodies (Thermo Fisher Scientific) were added at a 1:1000 dilution for 1 h at room temperature. Slices were washed again 3  $\times$  10 min with PBS, then stained with DAPI (Millipore Sigma, D9542) and mounted onto Fisherbrand Superfrost Plus Microscope Slides (Thermo Fisher Scientific, 12-550-15) with Fluoromount-G Slide Mounting Medium (VWR, 100502-406). Primary neurons cultured on cover glass were washed once with PBS, then fixed with 4% paraformaldehyde/PBS for 10 min at room temperature. Immunostaining proceeded as described.

Primary neurons cultured on poly-D-Lysine-coated coverslips (VWR, 194310012A) were washed once with PBS, then fixed with 4% paraformaldehyde/PBS for 10 min at room temperature. Immunostaining proceeded as described.

We stained for RAD21 with Anti-RAD21 antibody (Millipore, 05-908, 1:500 dilution), Lamin B1 with Anti-Lamin B1 antibody (Abcam, ab16048, 1:500 dilution), NeuN with Anti-NeuN antibody (Synaptic Systems, 266 004, 1:500 dilution), and  $\gamma$ -H2AX with Anti-phospho-Histone H2A.X antibody (Millipore, 05-636, 1:100 dilution) or anti-H2A.X-Phosphorylated (Ser139) antibody conjugated to APC (BioLegend, 613416). Mounted samples were imaged with Zeiss LSM 710 and 880 confocal microscopes. Images were quantified using ImageJ (NIH Image Analysis) and Imaris (Oxford Instruments). At least two coronal slices were used for each mouse for image quantification.

## QUANTIFICATION AND STATISTICAL ANALYSIS

### Smart-seq2 cell identities

For each of the 6,180 cells in the smart-seq2 dataset, we used HTSeq-count<sup>146</sup> on its filtered and recalibrated bam file to compute the cell's transcriptomic coverage over each gene's exons in GENCODE gene annotation (v28 lifted to b37). We used SCANPY<sup>147</sup> to process and cluster the expression profiles and infer cell identities. We kept only 19,765 protein-coding genes detected in at least 3 cells and filtered out 37 cells with less than 100 expressed genes. We identified and filtered out 322 additional cells showing very strong individual-specific batch effects, leaving 5,821 cells over 47 individuals. We used the filtered dataset to calculate the low dimensional

embedding of the cells (t-Stochastic Neighbor Embedding: t-SNE) (default parameters, perplexity = 50), built a nearest neighbors graph ( $n = 10$ ), and clustered it with the Louvain clustering (resolution = 2), giving 24 preliminary clusters. We then manually assigned clusters based on the following 2–3 major marker genes per class: Neuronal: GRIN1, SNAP25, SYT1; Excitatory neurons: CAMK2A, NRG1, SLC17A7; Inhibitory neurons: GAD1, GAD2; Astrocytes: AQP4, GFAP; Microglia: C3, CD74, CSF1R; Oligodendrocytes: MBP, MOBP, PLP1; Oligodendrocyte progenitor cells (OPCs): PDGFRA, VCAN; Endothelial: FLT1 and CLDN5. We merged clusters sharing marker genes to obtain 9 final clusters, defining two broad neuronal subtypes (1,170 excitatory and 221 inhibitory cells), four glial clusters (220 astrocytes, 255 microglia, 2121 oligodendrocytes, and 94 OPCs), 40 endothelial cells, 400 cells with strong individual-specific batch effect and cancer signatures (DNMT3A, COL6A3), and 1,300 senescent cells, marked by CARD8, FAM126A, IRX2, ALK, SENP7, and GMFB and lower overall transcription (Table S1, page 2).

For the 10x dataset, we collected 2,026,710 cells across 380 unique individuals in the ROSMAP cohort from Mathys et al. (in this issue).<sup>60</sup> We removed the 'SM\_171013Tsa' batch from the original dataset due to markedly lower quality, number of reads, and number of genes detected per cell. These batch effects were because this was the oldest batch in the collection and had been collected using 10x v2 chemistry as opposed to v3. The cell annotation was performed as described in Mathys et al. (in this issue)<sup>60</sup> and the resulting 2M cells contained 902k excitatory neurons (44.5% of cells). Differential expression analysis was performed in each excitatory neuron subtype separately at the pseudo-bulk level using Muscat for differential testing.<sup>148</sup>

### Gene fusions calling

For the human PFC Smart-seq2 and 10x datasets, we ran STAR-Fusion v1.10.1 on the GRCh37 genome and GENCODE v19 Mar012021 CTAT library with STAR version v2.7.3 but with the `-max-sensitivity` flag to collect all high-quality chimeric read alignments in each cell separately.<sup>112</sup> For 10x we removed any non-uniquely mapping reads, assigned each read to its corresponding barcode, and kept only those barcodes with cell assignments within the final set of 2M cells. We further filtered the human fusion calls by keeping unique breakpoints across all fusion calls and removing ribosomal and mitochondrial genes, immunoglobulin locus, pseudogenes, and MALAT1 (Table S1, page 3). Mouse Smart-seq2 data QC, quantification, cell type annotation, and pseudotime trajectory analysis is previously described in Welch et al., 2022. To re-align, call, and quantify gene fusions for each cell in this dataset separately, we ran STAR-Fusion v1.10.1 on the mm10 genome and GENCODE M24 Apr062020 CTAT library, with STAR version v2.7.3 and default parameters.<sup>59</sup> We further filtered the mouse fusion calls by removing fusions containing promiscuously chimeric lncRNA Shhg14 (Table S1, page 4).

### Gene fusions quantification

Quantification of fusions in the mouse Smart-seq2 analysis was performed both at the mouse and cell level, grouping all close fusions (<1Mb) and inter-chromosomal events. For human Smart-seq2 and human 10x data, we evaluated the relative contribution to detected fusion counts of the following individual-level variables: AD status (NIA-Reagan score 1–2 vs. 3–4, Braak stage 5–6 vs. 1–4, and AD cognitive impairment diagnosis 1–3 vs. 4–5), APOE e4 genotype, postmortem interval (PMI, in units of 10 h), age of death (in units of 10 years). We quantified the enrichment of putative fusion events at the cell level across conditions using a negative binomial generalized linear model where we model the number of fusions in each cell with an offset term for the number of reads captured for that cell ( $\log(n\_counts)$ ). We include as cell-level covariates the cell type (if not evaluating on a single cell type), the number of captured genes ( $\log(n\_genes)$ ), and the number of reads per gene. As individual-level variables, we include sex, age of death (rescaled by dividing by 10), and PMI (also rescaled by a factor of 10). We adjust the resulting p values using the Benjamini-Hochberg method (BH in `p.adjust` in R). Regression coefficient plots show regression estimates plus or minus  $2^*SE$  on either side.

Gene set signatures were built by taking all unique genes in GO terms containing the relevant keywords (senescence, repair, DNA damage, synapse, neuron) from MGI (mouse, 2022-08-06) and GO (human, 2019-11-02). In CK/CK-p25 mouse analysis, Step 2 and Step 1 signatures are as previously described.<sup>58</sup> Gene set signatures in each cell were computed as the sum of expression of all constituent genes (TP10k),  $\log_1p$  transformed, z-scored, and cells stratified into high ( $Z$  score >1) and low ( $Z$  score  $\leq 1$ ) signature expression for comparison with fusions. For the cell-level stratified gene signature scores we performed the same regression analysis as for the human individual-level variables and included the same cell and individual-level covariates.

For gene-level tests, we aggregated putative fusions in each gene across all individuals in the 10x cohort. We tested the contribution of various gene-level labels on the number of fusions in each gene by a negative binomial generalized linear model. We tested whether the gene was in the RDC gene set, in the AD GWAS gene set, or whether their length or expression ( $\log$ -transformed), contributed to the number of fusions. We tested the GWAS association using both a reduced set of 91 prioritized genes and an expanded set of 1329 genes covering the majority of genes in GWAS loci.<sup>74</sup>

### Mate-pair seq analysis

Mate-pair paired-end fastq reads were trimmed using cutadapt to remove any Illumina adaptors. The paired reads were aligned separately to the mm10 genome using bowtie2 with a quality score above 10.<sup>143</sup> Mapped reads were converted to bam files using samtoolsView in samtools. The bam files were filtered for PCR duplicates using samtools Rmdup and converted to bed files using bamtoBed in bedtools. Bed files from corresponding paired fastq files were merged to make pair files for each sample.

### BLISS data analysis

BLISS fastq reads were demultiplexed into individual sample fastq reads based on sample-specific barcodes. The reads were filtered based on Unique Molecular Index (UMI) to remove PCR duplicates. The resulting fastq files were trimmed to remove any sample barcodes using cutadapt (<https://cutadapt.readthedocs.io/en/stable/>). The reads were aligned to the mm10 genome using bowtie2 with a quality score above 10.<sup>143</sup> Mapped reads were converted to bam files using samtoolsView in samtools, then aggregated into bed files using bamtoBed in bedtools.<sup>145</sup> These steps were performed using R wrapper scripts from the R trAVIS package (<https://github.com/dvera/travis>). Bed files binned into 0.5 kb windows were used for the visualization of data using Integrative Genomics Viewer (IGV).

### Oxford nanopore Technology (ONT) sequencing analysis

We filtered ONT reads for complete, non-chimeric 10x cDNA products with appropriate flanking primers following Lebrigand et al., 2020.<sup>142</sup> We mapped reads to the hg38 genome using minimap2 (v2.22-r1101) with parameters “-ax splice -uf -MD -sam-hit-only -t 20 -junc-bed” and junction bed file built from the GENCODE v28 release with additional scaffolds.<sup>149</sup> We added overlapping gene and sequence tags and extracted reads with clipped alignments over genic regions. We remapped these with “-ax splice -k 13 -t 20” and the same junction file. To scan for fusion events, we filtered the resulting alignments with sam flags “-F 1792 -f 2048” to keep reads whose primary alignment passed QC and was tagged with supplementary alignments. We further filtered to reads with alignments over coding regions and removed any malformed or chimeric reads remaining. We sorted the alignments by alignment quality and alignment edit distance to visualize examples, which we further confirmed by running Blast on the original reads.

### Hi-C analysis

Hi-C was analyzed using the HOMER Hi-C analysis pipeline (<http://homer.ucsd.edu/homer/interactions2/index.html>)<sup>91</sup> and Juicer.<sup>88,144</sup> A/B compartment scores and changes in compartment scores were computed using HOMER default settings with a resolution of 25 kb. For Control and Step 1 neurons, all three bio-replicates were used for the calculation of statistical significance, and for Step 2 neurons bio-replicates 2 and 3 were used. Bio-replicate 1 of Step 2 neurons was excluded from the analysis of differential A/B compartment statistical significance owing to its lower read depth. Compartment bins were marked as differentially regulated if there was a magnitude change of greater than 0.5 along with a sign change and an adjusted p value <0.05. TADs and Loops were called using HOMER default settings with -res 3000 -window 15000 and -res 10000 -window 25000 and merged. (Table S1 pages 9, 10). For low-resolution Hi-C from primary neuronal cultures and P301S Tau mice, TADs were called using -res 25000 -window 50000, and loops were called using HOMER setting -res 10000 -window 25000 (Table S1, pages 11–13), and Juicer tools were used to visualize Hi-C heatmaps and create aggregate plots of loops.

### Gene ontology analysis

Gene ontology analysis in Figure 5C was performed using GOrilla<sup>155</sup> with two unranked lists of genes, downregulated genes (adj. p value <0.05, log<sub>2</sub> (fold change) > 1), and all expressed genes. Only GO terms with adj. p value <0.01 in at least Step 1 or Step 2 were kept.

### Human RAD21 staining analysis

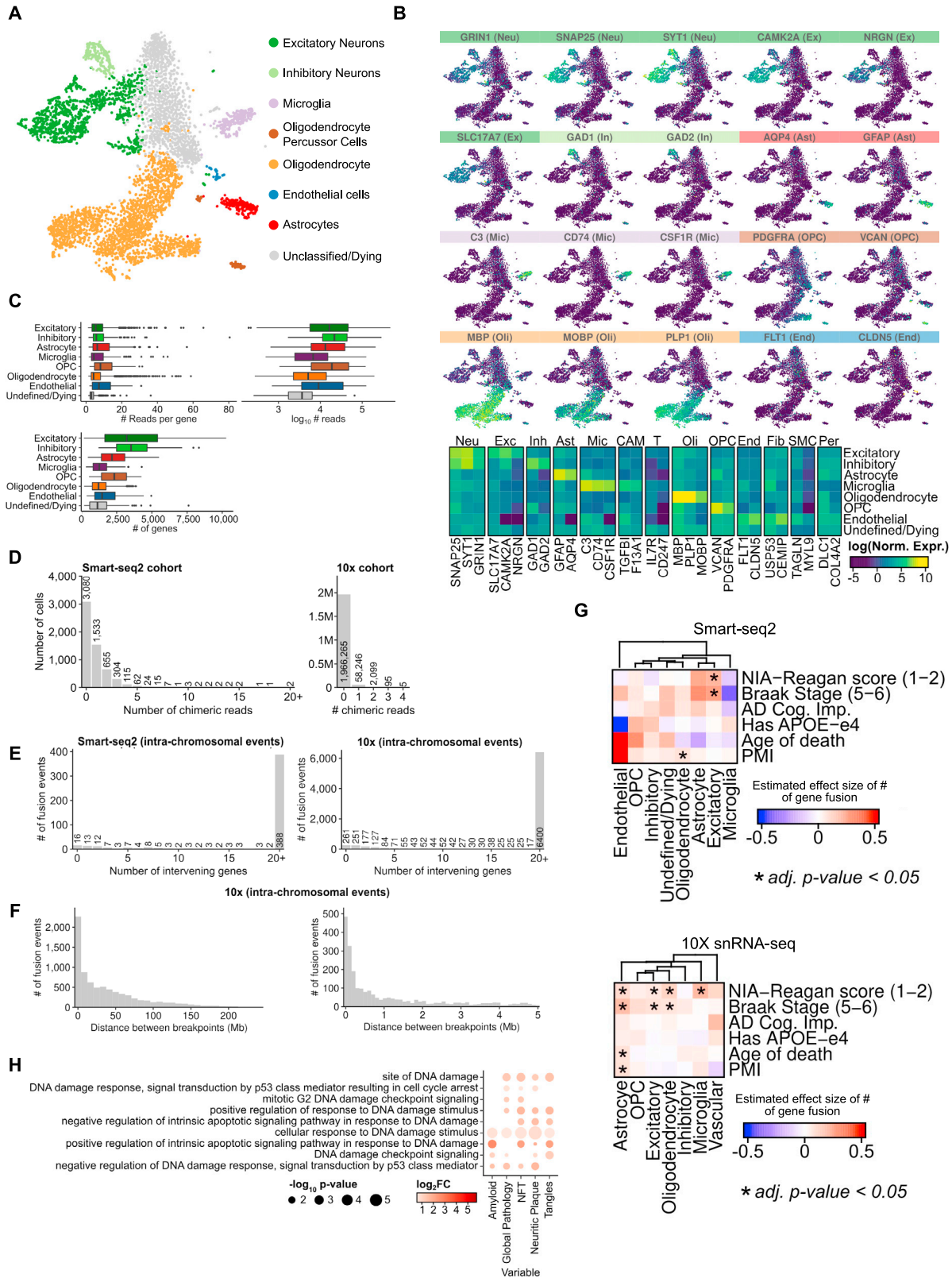
To assess the differences in RAD21 values between control and Alzheimer’s disease (AD) individuals, we employed a linear mixed-effects model using the lme4 package in R.<sup>156</sup> The dataset consisted of RAD21 mean intensity values measured in each neuron and the percentage of neurons with high RAD21 (>50th percentile) per image from both control and AD individuals. We fitted a linear mixed-effects model with the percentage of high RAD21 neurons or mean intensity of RAD21 as the response variable, group (Control or AD) as the fixed effect, and individual (ID) as the random effect. To test the significance of the group effect, we performed a likelihood ratio test comparing the full model (with the group effect) against a null model excluding the group effect.

### ADDITIONAL RESOURCES

We have established a web portal for this paper at [http://compbio.mit.edu/ad\\_dna\\_damage/](http://compbio.mit.edu/ad_dna_damage/) to better describe and provide access to our datasets and code.



# Supplemental figures

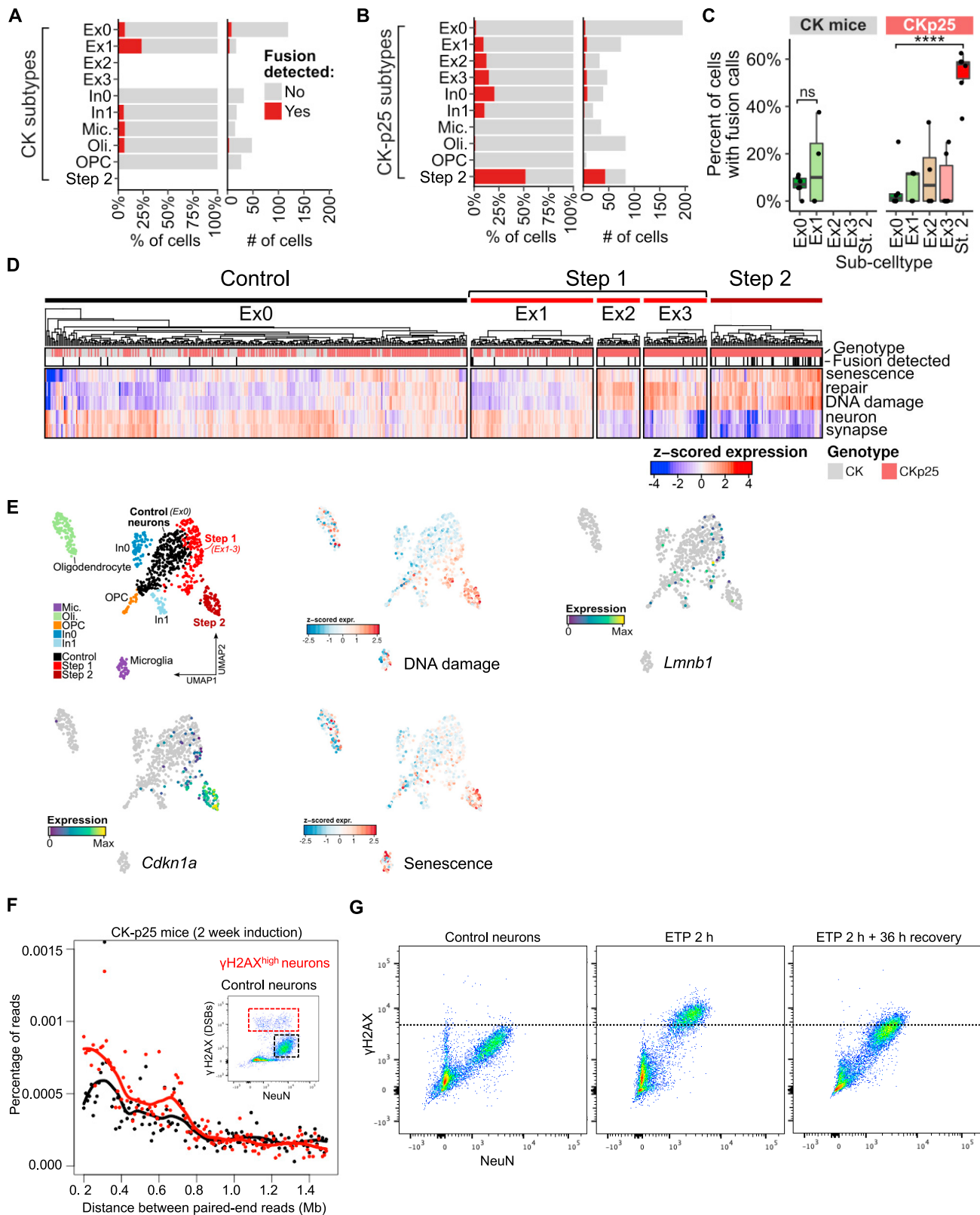


(legend on next page)

---

**Figure S1. Smart-seq2 and 10X snRNA-seq gene fusion calling in human postmortem brain samples, related to Figure 1**

- (A) UMAP for Smart-seq2 from postmortem human PFC, colored by cell-type.
- (B) Expression of cell-type-specific markers (top). Heatmap of cell-type-specific markers in each cluster (bottom).
- (C) Boxplots of QC metrics in each cell cluster in Smart-seq2.
- (D) Histogram of the number of chimeric reads identified per cell.
- (E) Histogram of the number of intervening genes between pairs of fused genes.
- (F) Histogram of the distance between pairs of fused genes.
- (G) Heatmap of gene fusions (effect size) for human subject covariates against cell types (\*adjusted p value < 0.05). Covariates include AD cognitive impairment and postmortem interval (PMI).
- (H) Enrichment of excitatory neuron up-regulated DEGs for various AD ascertainment variables in DNA damage gene ontology terms (hypergeometric test, terms with  $p < 0.05$  and with more than one associated diagnosis shown).



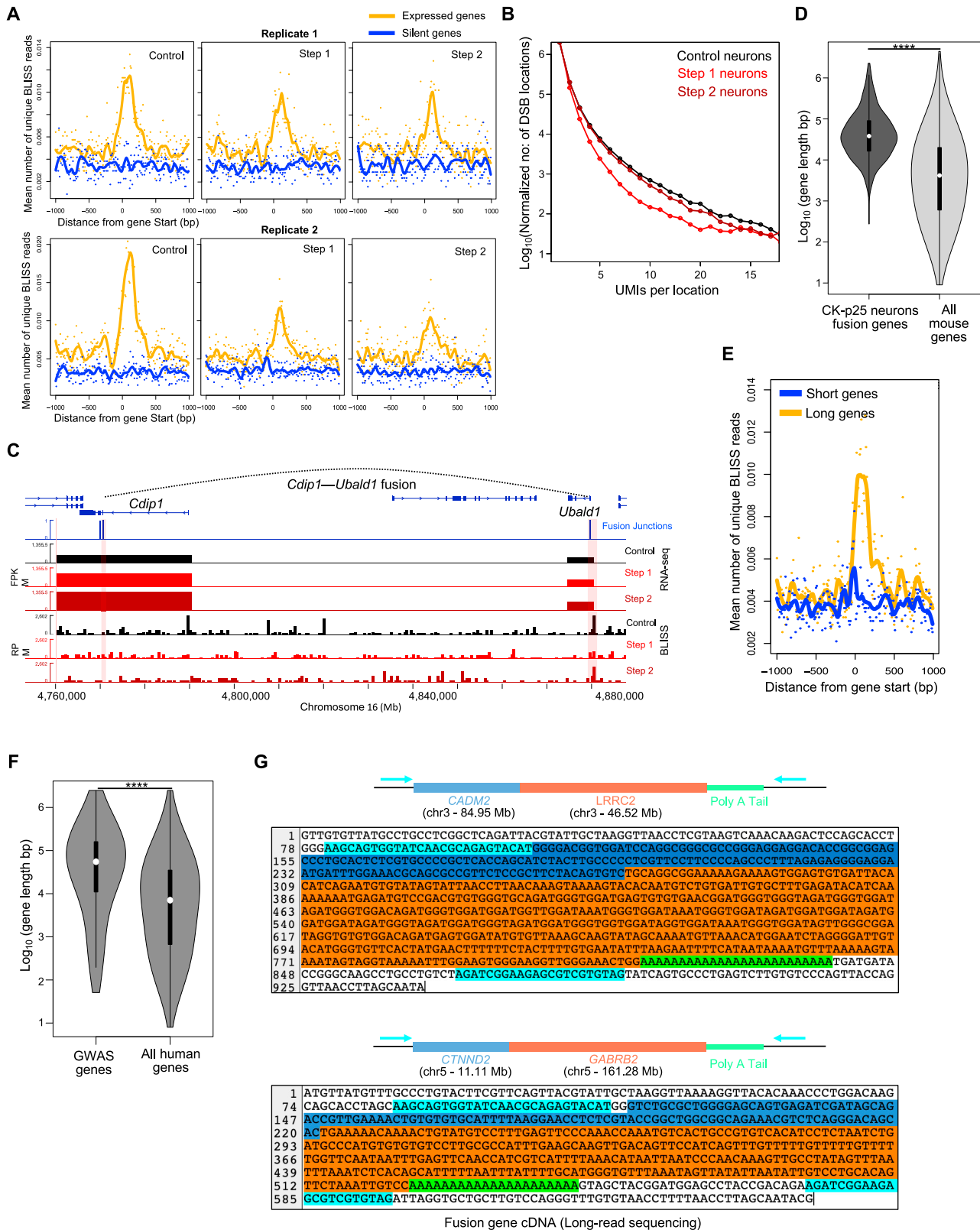
(legend on next page)

---

**Figure S2. Step 2 neurons with senescence signature have increased gene fusions and genome structural variations, related to Figure 1**

- (A) Fraction and number of cells with or without at least one gene fusion in each cell type in snRNA-seq in CK mice.
- (B) Same as panel A, for CK-p25 mice.
- (C) Percent of cells with at least one gene fusion at the mouse level in Control, Step 1, and Step 2 neurons (t-test). Each dot represents one animal.
- (D) Expression (z-scored) of genes in gene ontology terms with specific keywords (senescence, DNA damage, repair, neuron, synapse) across all single cells from Control, Step 1, and Step 2 neurons. Cells with at least one gene fusion detected are marked by a black line.
- (E) Overlay of *Cdkn1a* gene expression, *Lmnb1* gene expression, senescence gene set Z score, and DNA damage gene set Z score on UMAP.
- (F) Percentage of mate-pair sequencing read pairs separated by large genomic distances (>200 kb), indicating genome structural variation events.
- (G) FANS dot-plot of neuronal culture after vehicle (DMSO), etoposide (2 h), and etoposide recovery (2 h ETP +36 h recovery) using NeuN (neuron) and  $\gamma$ H2AX (DSB) marker.





(legend on next page)

---

**Figure S3. Long and highly expressed genes have increased DSBs and a higher propensity for gene fusions, related to Figure 2**

(A) Aggregate plots of BLISS reads centered at gene starts for the top 2500 expressed (yellow) and the bottom 2500 silent genes (blue), for Control, Step 1, and Step 2 neurons in both replicates.

(B) Number of DSBs ( $\log_{10}$ , normalized) for each number of supporting UMIs (BLISS data).

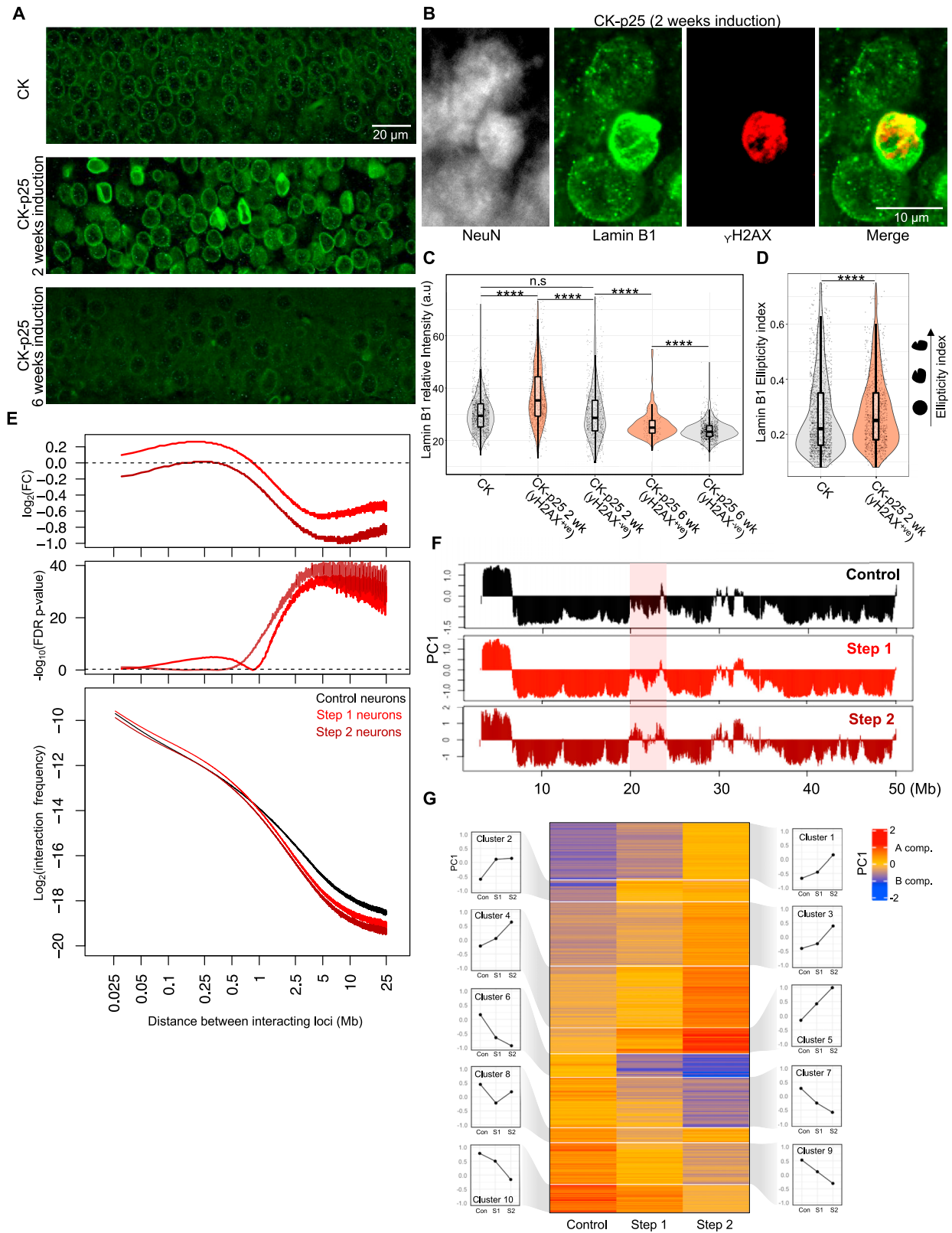
(C) Genome browser snapshot of example gene fusion in CK-p25 mice Step 2 neurons. Panels show fusion junctions (top), bulk RNA-seq signal (panels 2–4), and BLISS in the three populations (panels 5–7).

(D) Gene lengths of fusion genes called in CK-p25 excitatory neurons versus all mouse genes (Wilcoxon test, \*\*\*\* $p < 1e-4$ ).

(E) Aggregate plots of BLISS reads centered at gene starts for the top 2500 longest genes (yellow) and the bottom 2500 shortest genes (blue), for Control neurons.

(F) Gene lengths of GWAS genes compared to all human genes (Wilcoxon test).

(G) Complete long-read sequences of fusion gene examples from Figure 2G.



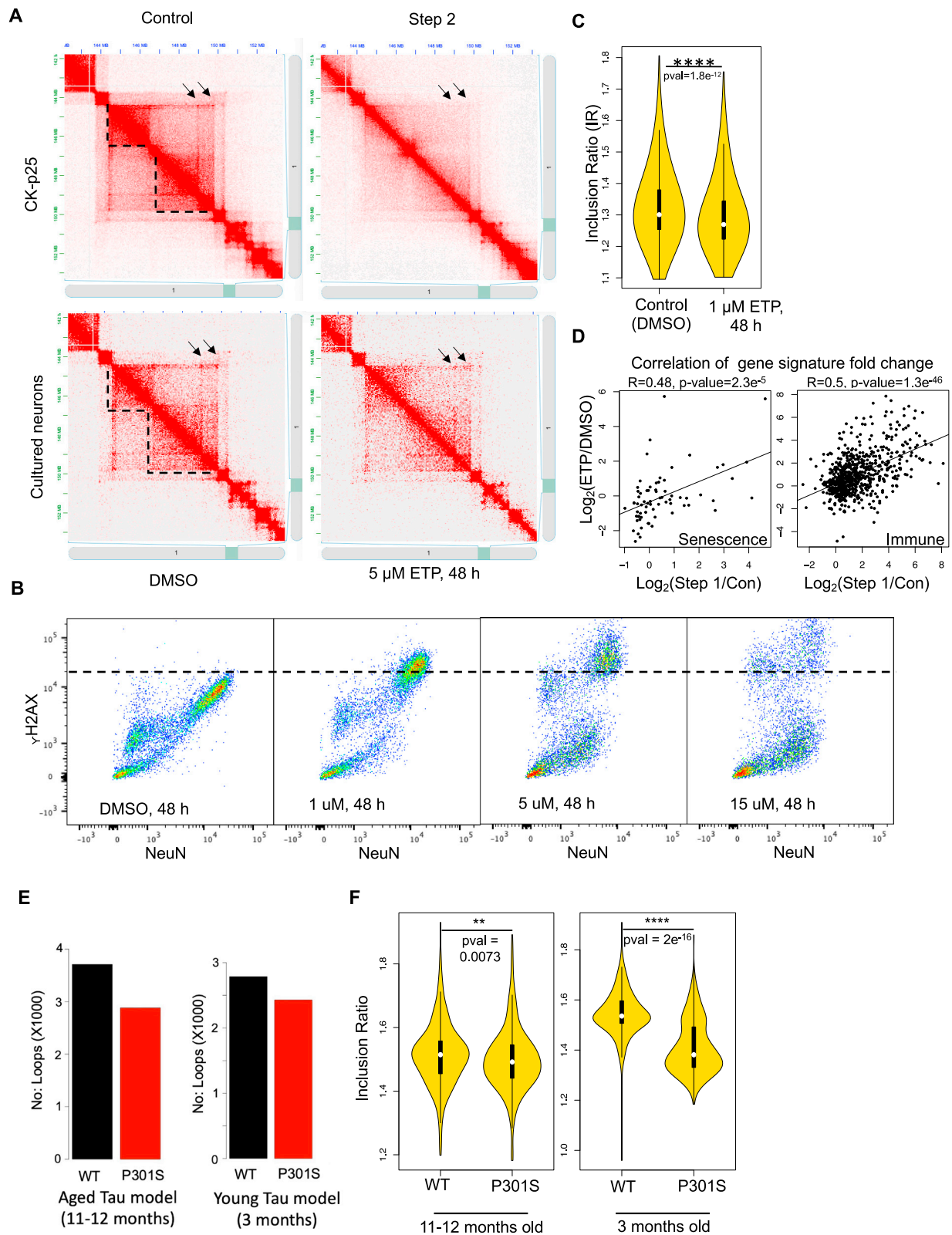
(legend on next page)

---

**Figure S4. 3D genome organization is disrupted in neurons harboring DSBs, related to Figure 3**

- (A) Representative immunohistochemistry images and quantification of Lamin B1 in 2-week and 6-week induced CK-p25 mice in the dentate gyrus.
- (B) Representative higher magnification images comparing neurons with baseline DSBs to neurons enriched for DSBs.
- (C) Violin plots quantifying Lamin B1 mean intensity in neurons enriched for  $\gamma$ H2AX and neurons with baseline  $\gamma$ H2AX in CK/CK-p25 mice (Wilcoxon test with Benjamini–Hochberg correction, \*\*\*\* $p < 1e-4$ ).
- (D) Violin plots quantifying Lamin B1 ellipticity in neurons from control CK mice and neurons enriched for  $\gamma$ H2AX from CK-p25 2-week induction (Wilcoxon test).
- (E) Distance decay of chromatin interaction frequency measured by Hi-C as a function of the distance between the interacting loci for Control, Step 1, and Step 2 neurons. Log<sub>2</sub> fold change and significance between Step 1 and 2 vs. Control neurons are shown in the top two panels.
- (F) Representative plot showing A/B compartmentalization (principal component 1) measured by Hi-C in Control, Step 1, and Step 2 neurons.
- (G) K-means clustering of A/B compartmentalization (PC1) across Control, Step 1, and Step 2 neurons.





(legend on next page)

---

**Figure S5. DSBs are sufficient to disrupt the 3D genome organization in neurons, related to Figure 4; Table S1, pages 12 and 13**

- (A) Representative Hi-C heatmaps comparing the disruption of 3D genome organization in etoposide-treated primary neurons to CK-p25 neurons.
- (B) FANS dot-plot of neuronal culture after etoposide (different concentrations) or vehicle (DMSO) treatment using NeuN (neuron) and  $\gamma$ H2AX (DSB) marker.
- (C) Quantification of the TAD disruption through Inclusion Ratio (IR) (Wilcoxon test, \*\*\*\*  $p < 1e-4$ ).
- (D) Correlation of differentially expressed senescence and immune-related genes between Etoposide treatment (25  $\mu$ M for 6 h) and CK-p25 (Welch et al.,<sup>58</sup> RNA-seq).
- (E) Number of chromatin loops from Hi-C in P301S Tau model in both young (3 months) and old (11–12 months) animals.
- (F) TAD disruption (IR) in the P301S Tau model in both young (3 months) and old (11–12 months) animals (Wilcoxon test).

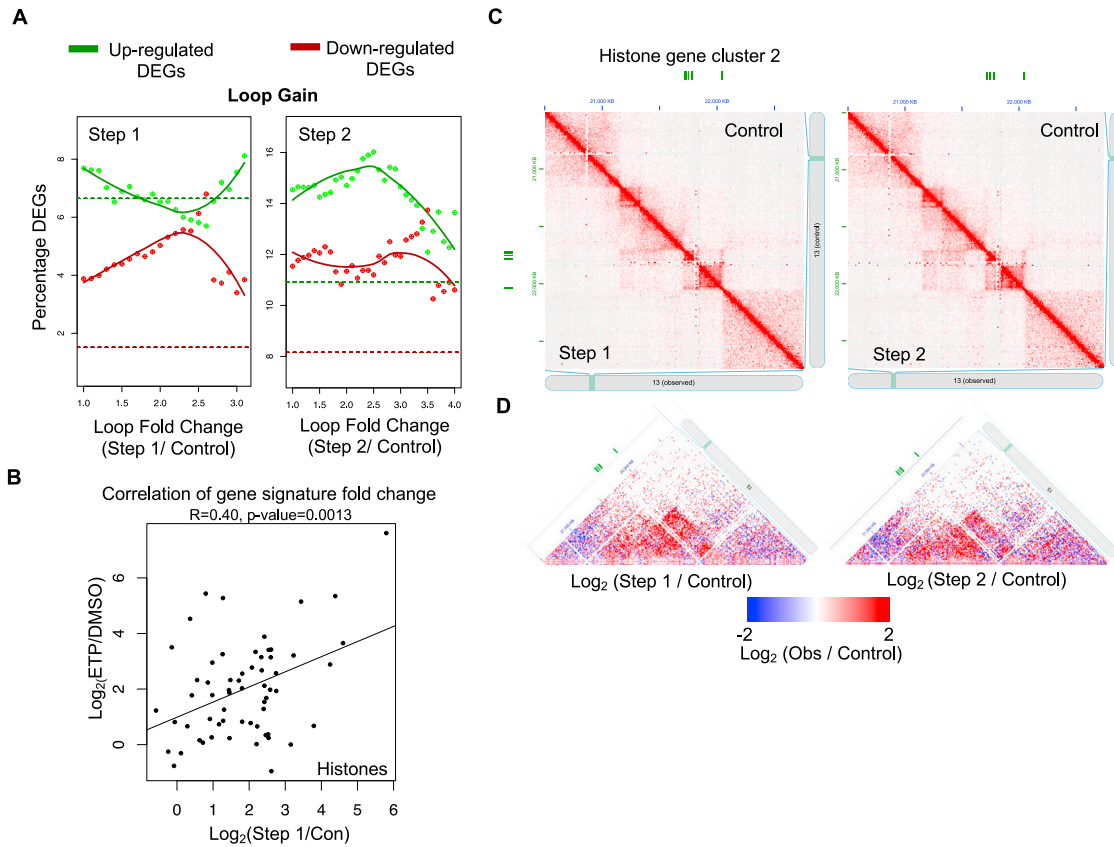


**Figure S6. Re-organization of the 3D genome aligns with gene expression changes, related to Figures 5 and 6**

(A) Percentage of up and down DEGs vs. loop fold change for loop gain. Colored dotted lines represent baselines (genome-wide percentage of DEGs).

(B) Correlation of differentially expressed histone genes between Etoposide treatment (25  $\mu\text{M}$  for 6 h) and CK-p25 (Welch et al.,<sup>58</sup> RNA-seq).

(C) Hi-C interaction matrix for second histone gene cluster (green blocks, chr13). The lower diagonal is Step 1 or 2, upper is Control.

(D) Differential Hi-C heatmaps comparing Step 1/Control and Step 2/Control, colored by increased (red) or decreased (blue) interactions over control. Hi-C heatmaps were rotated 45° and only the upper triangle is shown.